LBL-23057 c.2

Lawrence Berkeley Laboratory
UNIVERSITY OF CALIFORNIA

Materials & Chemical Sciences Division

MAY 12 1987
DOCUMENTS SECTION

MICROSTRUCTURE AND CREEP FAILURE OF SILICON CARBIDE

G.H. Campbell
(M.S. Thesis)

December 1986

TWO-WEEK LOAN COPY
This is a Library Circulating Copy which may be borrowed for two weeks

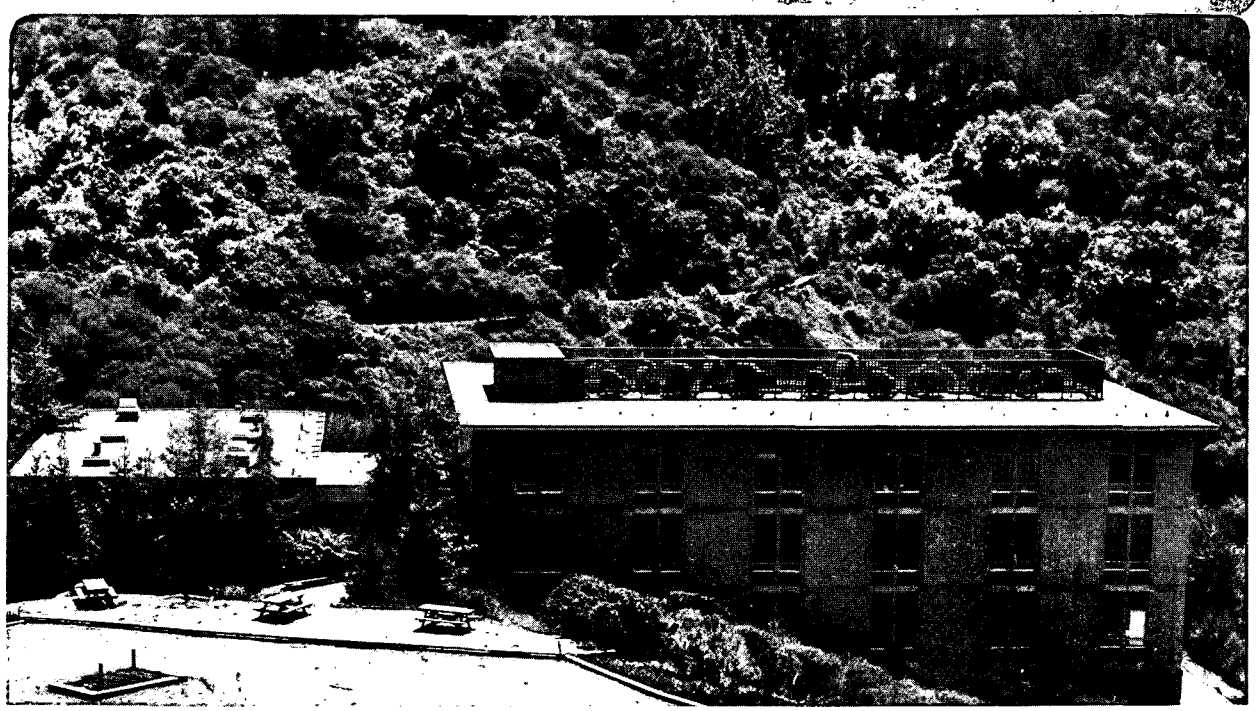

LBL-23057 c.2

Prepared for the U.S. Department of Energy under Contract DE-AC03-76SF00098

DISCLAIMER

This document was prepared as an account of work sponsored by the United States Government. While this document is believed to contain correct information, neither the United States Government nor any agency thereof, nor the Regents of the University of California, nor any of their employees, makes any warranty, express or implied, or assumes any legal responsibility for the accuracy, completeness, or usefulness of any information, apparatus, product, or process disclosed, or represents that its use would not infringe privately owned rights. Reference herein to any specific commercial product, process, or service by its trade name, trademark, manufacturer, or otherwise, does not necessarily constitute or imply its endorsement, recommendation, or favoring by the United States Government or any agency thereof, or the Regents of the University of California. The views and opinions of authors expressed herein do not necessarily state or reflect those of the United States Government or any agency thereof or the Regents of the University of California.

Microstructure and Creep Failure of Silicon Carbide

Geoffrey Hays Campbell

M.S. Thesis

Lawrence Berkeley Laboratory
University of California
Berkeley, California 94720

This work was supported by the U.S. Department of Energy under Contract Number DE-AC03-76SF00098.

ABSTRACT

Observations of the microstructure and creep behavior of two commercial silicon carbides are presented. A combination of techniques has been used to characterize the microstructure. Sequential creep rupture testing has been carried out in an inert environment at varied temperatures and strain rates, and scanning electron microscopy has been used to observe creep crack propagation and damage development with increasing strain. Basic theory is developed for stress fields and creep rates around a crack tip and is related to the observed brittle to ductile transition in the material as well as room temperature behavior of deformed beams.

Acknowledgement

I would like to express my deepest thanks to Dr. Brian Dalgleish. His broad experience and experimental expertise contributed greatly to this research. All of the TEM photos in this report are his as well as Figures 9, 12, and 16 and the X-ray spectra. I would also like to thank Professor Tony Evans. His insight allowed us to put the analysis of the results to be put in proper mathematical form.

TABLE OF CONTENTS

	Page
Abstract	i
Acknowledgement	ii
Table of Contents	iii
List of Figures	iv
1. INTRODUCTION	1
2. MATERIALS	9
2.1 Processing Conditions	9
2.2 Specimen Preparation	10
2.3 Characterization Techniques	10
2.4 Material Characteristics	11
i. Hot-Pressed Silicon Carbide	11
ii. Sintered Silicon Carbide	21
3. MECHANICAL PROPERTIES	29
3.1 Techniques	29
3.2 Basic Theoretical Results	31
3.3 Properties	36
4. DISCUSSION	42
4.1 The Flow Stress	47
4.2 The Fracture Stress	50
5. CONCLUSIONS	53
REFERENCES	54

LIST OF FIGURES

		Page
1.	Schematic indicating crack growth and creep damage controlled regimes of creep rupture and associated blunting threshold (courtesy B. Dalgleish)	2
2.	Scanning Electron Micrograph of blunt crack formed by loading at stress intensities below threshold (courtesy W. Blumenthal)	3
3.	Crack tip velocity as a function of normalized stress intensity factor for alumina at 1300 and 1400C (courtesy W. Blumenthal)	4
4.	Schematic of stress for competing processes of flow and fracture	6
5.	Crack tip velocity as a function of normalized stress intensity factor for Si_3N_4 showing decrease of blunting threshold with increasing glass content (courtesy B. Karunaratne and M. Lewis)	8
6.	Backscatter electron micrograph of as-polished surface of hot-pressed silicon carbide	14
7.	X-ray spectra from microprobe of two second phase inclusions	15
8.	Transmission electron micrograph of hot-pressed silicon carbide showing large amounts of second phase	16
9.	Scanning electron micrograph of thermally etched hot-pressed silicon carbide showing presence of large scale inhomogeneities and glassy ligaments	17
10.	Scanning electron micrograph of thermally etched hot-pressed silicon carbide showing migration of second phase to surface	18

LIST OF FIGURES (Continued)

Page

11. a-b) X-ray spectra of two different second phase particles in the hot-pressed silicon carbide---------- 19-20

12. Dot maps of second phase particles in hot-pressed material---------- 22

13. (a) Transmission electron micrograph of sintered silicon carbide showing residual carbon; (b) electron energy loss spectra identifying the residual carbon as graphite- 23

14. Transmission electron micrograph of sintered silicon carbide showing graphite inclusions- 24

15. Scanning electron micrograph of an as-fractured surface of sintered silicon carbide showing laminar structure of graphite inclusion---------- 25

16. Scanning electron micrograph of as-polished surface of sintered silicon carbide showing metal silicide inclusions at C---------- 26

17. X-ray spectra of metal silicide inclusion in sintered silicon carbide---------- 27

18. Plot of $\sigma_{\theta\theta}$ at $\theta = 0$ for a blunt crack in a creeping material for different values of the creep exponent---------- 32

19. Plot of σ_{yy} in front of a blunt notch for differing values of the crack opening displacement---------- 35

20. Schematic stress-strain curve showing brittle to ductile transition in hot-pressed silicon carbide---------- 38

21. Schematic stress-strain curve showing brittle to ductile transition in sintered silicon carbide---------- 39

LIST OF FIGURES (Continued)

Page

22. Scanning electron micrograph of an indentaion crack tip at increasing strain in sintered silicon carbide---------- 43

23. Scanning electron micrograph of region in front of an indentation crack in a strained beam of sintered silicon carbide showing cavity formation at a graphite inclusion---- 44

24. Scanning electron micrograph of an indentation crack in hot-pressed silicon carbide at 5 and 10% strain---------- 45

25. Scanning electron micrograph of cavitation in front of a crack tip in hot-pressed silicon carbide---------- 46

26. Plot of strength vs temperature and flow stress vs temperature for hot-pressed SiC--- 48

27. Plot of strength vs temperature and flow stress vs temperature for sintered silicon carbide---------- 49

28. Schematic stress strain curve for constant displacement rate creep test---------- 52

1. INTRODUCTION

The high temperature failure of ceramics has been shown to involve two predominant regimes: high stress ruptures by the extension of pre-existing cracks and low stress fractures that occur by damage accumulation (Fig. 1). The transition between regimes coincides with a relatively abrupt change in rupture strain (Fig. 1) and is accompanied by the creep blunting of pre-existing flaws (Fig. 2). Some aspects of the blunting transition have been studied for various Al_2O_3,[1-6] SiC[7-10] and Si_3N_4[11] materials. However, present understanding of this vitally important aspect of creep rupture is still speculative. The prevalent speculation is that blunting occurs when the stress and displacement field ahead of the crack reduces below a threshold value, at which the nucleation of a crack tip damage zone (i.e. cavities at grain boundaries and/or in amorphous phases) is suppressed, resulting in a threshold stress intensity, K_{th} (Fig. 3).

At stress intensities below K_{th}, rupture occurs by damage accumulation. For Al_2O_3, failure in this damage controlled regime has been shown to occur by the growth and coalescence of shear bands that nucleate at large microstructural and chemical heterogeneities within the material.[1-6] When such mechanisms are suppressed, by

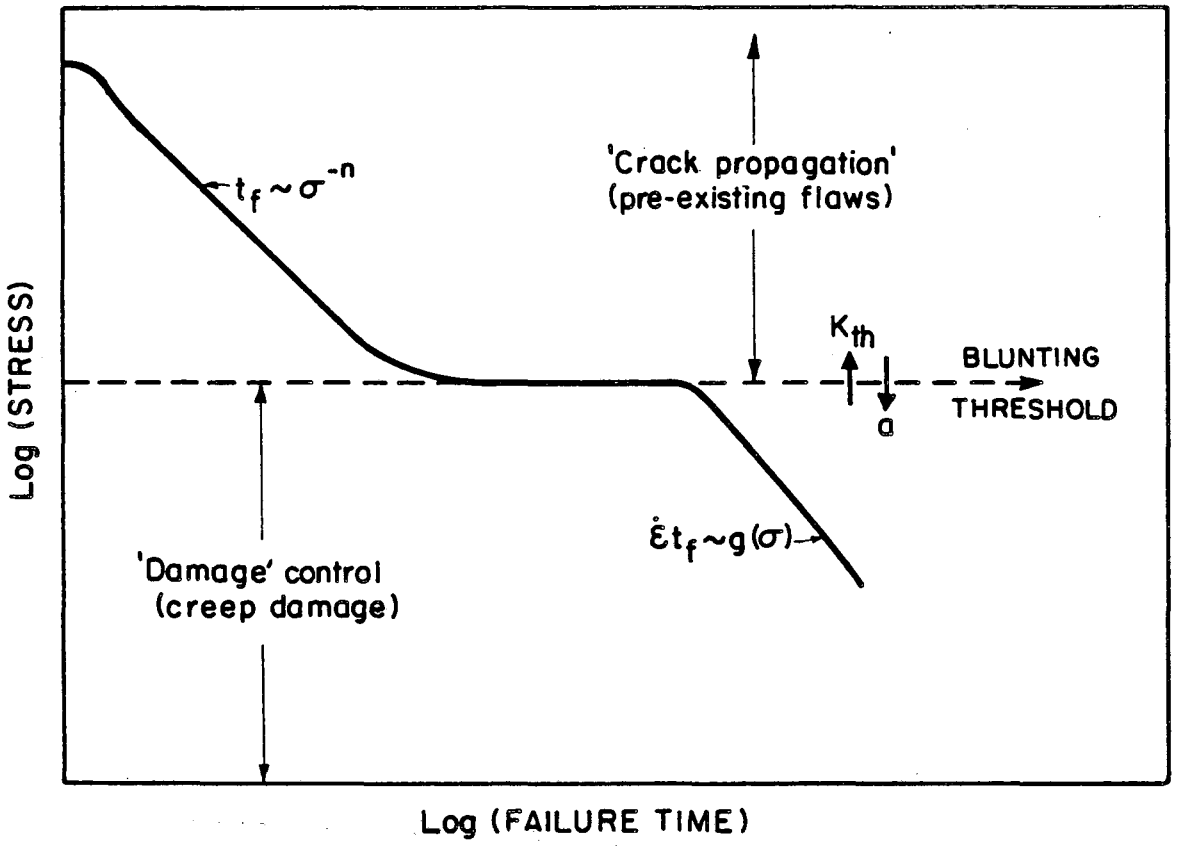

XBL 853-1578

FIG. 1

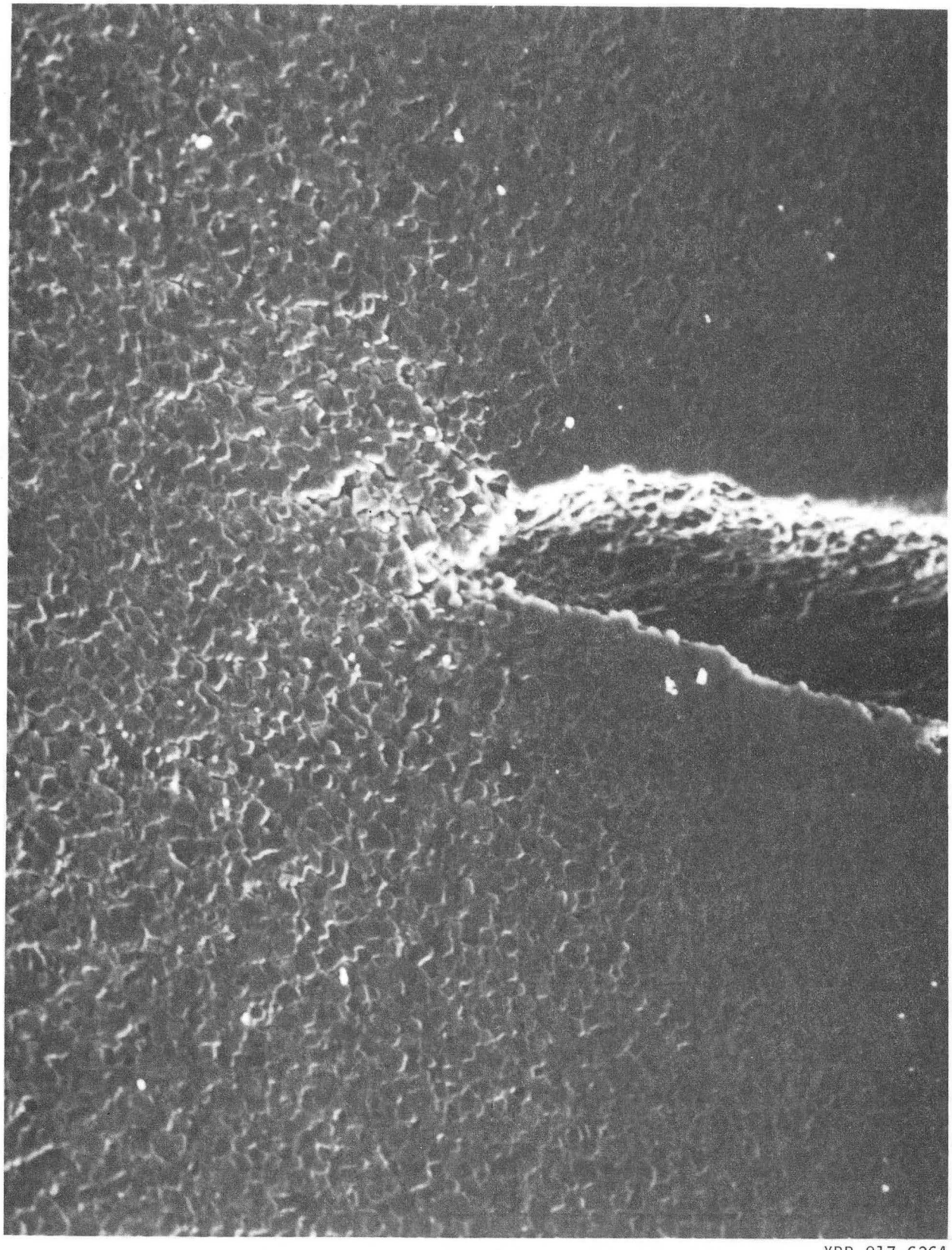

FIG. 2

XBB 817-6364

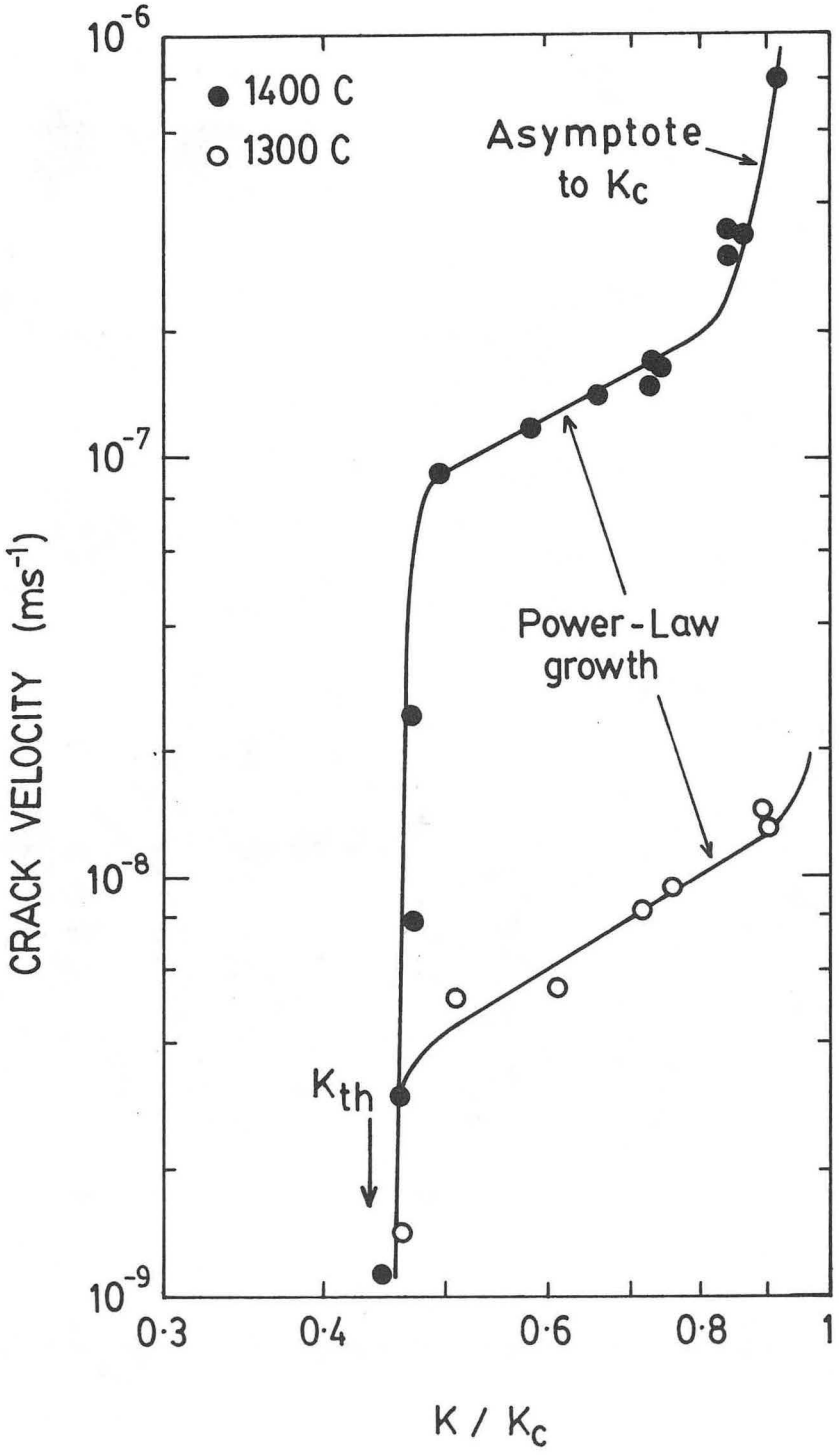

XBL 847-2859

FIG. 3

having superior microstructural and chemical homogeneity,[12] alternative failure processes can be expected. Indeed, recent research on ZrO_2[13] (TZP) and Al_2O_3/ZrO_2 composites[14-16] indicates that, in some cases, sufficient damage does not occur below the blunting threshold and the material then becomes superplastic.

The abrupt change in rupture behavior around the blunting threshold can be regarded as a transition from creep brittleness to creep ductility, involving a competition between flow (creep) and fracture, as depicted schematically in Fig. 4. The rupture characteristics ascertained for constant strain-rate conditions should thus exhibit a transition temperature, T_t, below which the material fails at small strains (by crack growth from pre-existing flaws) and above which creep ductility obtains, with failure proceeding by damage mechanism.

The intent of the present research is to examine aspects of the brittle-to-ductile transition for two SiC materials, as needed to further understand this important phenomenon. Some prior research on SiC[7-10] has provided indirect evidence of a blunting threshold, that varies with temperature, microstructure and environment. This research has also suggested that both the threshold and the creep crack growth above the threshold are dominated by the presence and the characteristics of amorphous

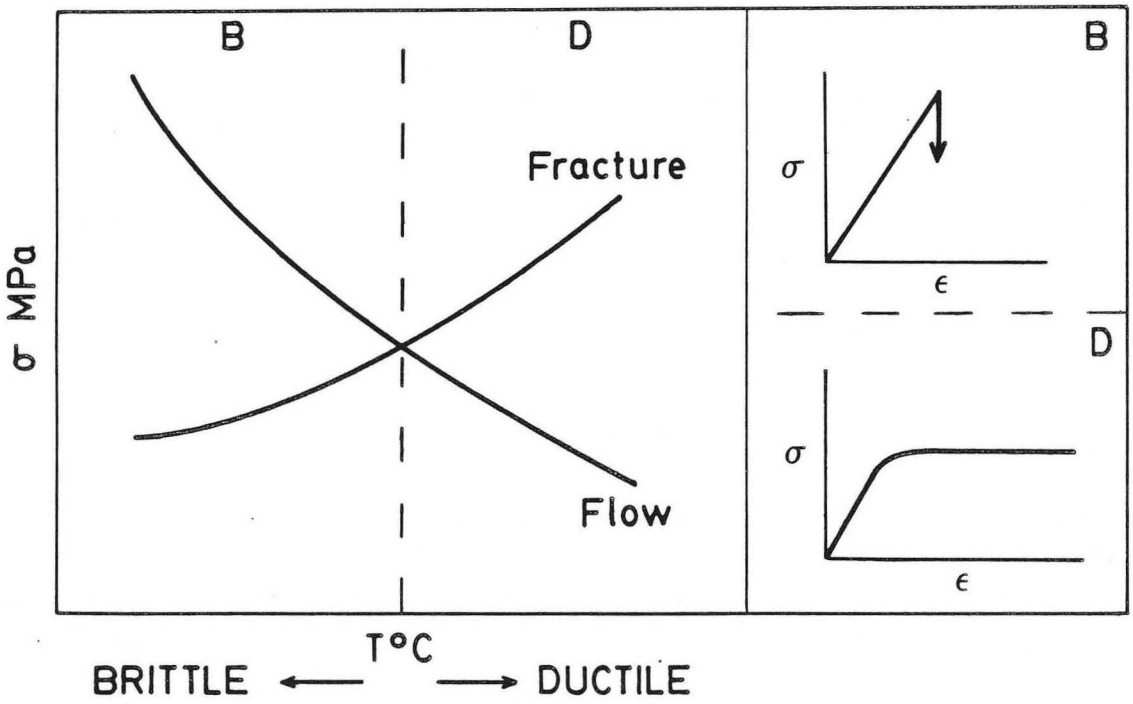

XBL 869-3243

FIG. 4

grain boundary phases that either pre-exist or are formed by exposure to oxidizing environments. Specifically, low viscosity and low surface energy amorphous phases accelerate the crack growth and reduce the relative blunting threshold, K_{th}/K_c, (as also established for various Al_2O_3[1-6] and Si_3N_4[11] materials, Fig. 5). The present research is performed in an inert environment in an attempt to preserve the initial phase characteristics during testing.

An important constituent of the current research is the thorough characterization of the materials and the direct observation of crack blunting and of damage. These aspects of the research are presented first, followed by measurements of mechanical behavior and interpretation of the brittle to ductile transition.

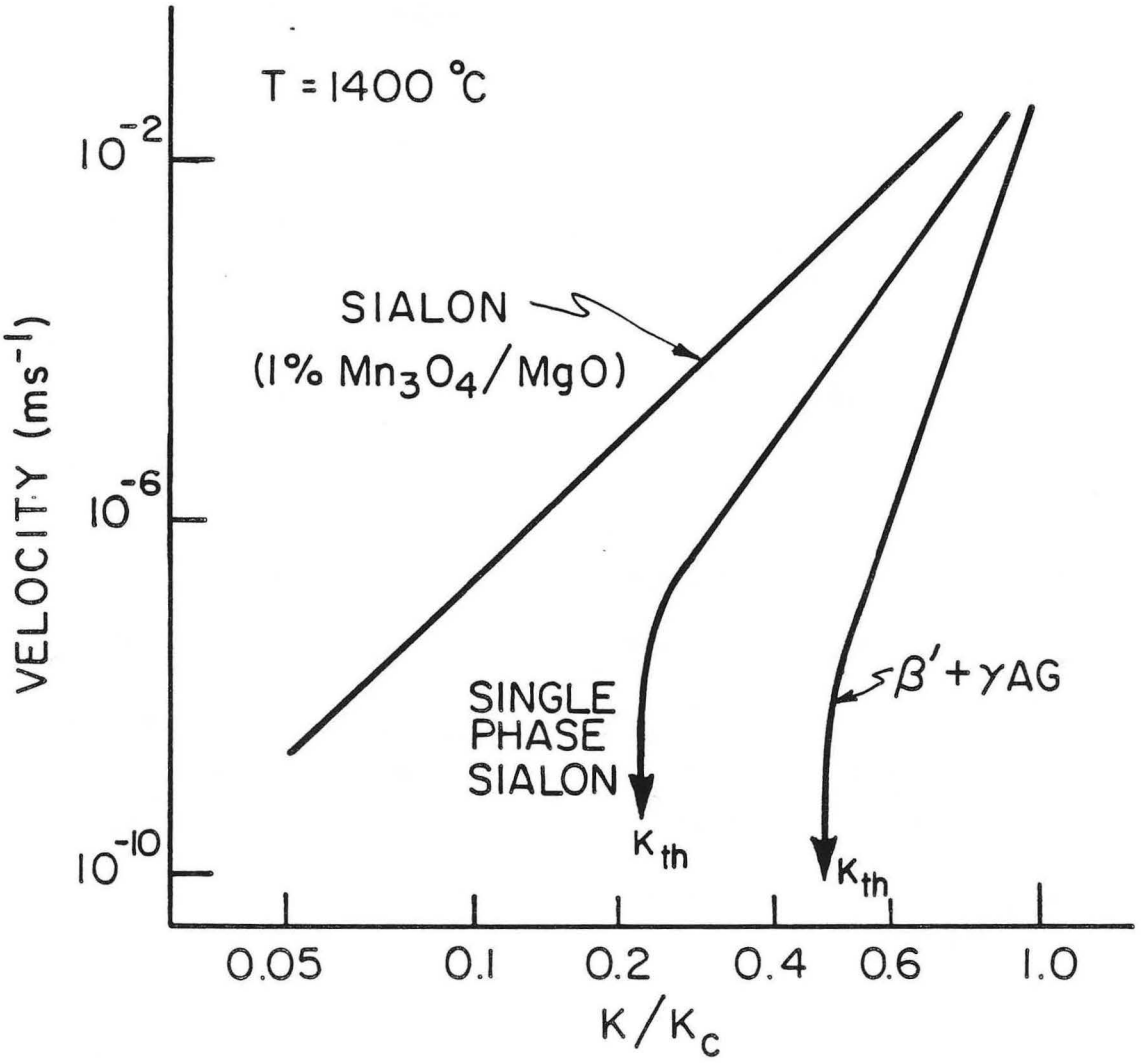

XBL 816-6003

FIG. 5

2. MATERIALS

2.1 Processing Conditions

One silicon carbide* was manufactured[17] by mixing a fine, high purity silicon carbide powder with 0.5-5 wt% aluminum in a ball mill, using cobalt bonded tungsten carbide grinding media and hot-pressed at 2075°C and 18 MPa. The other material** was a sintered α-SiC containing boron and excess carbon as sintering aids.[18] The silicon carbide powder containing excess carbon was mixed with boron carbide powder in a ball mill using tungsten carbide balls. It was sintered at 2100°C in an atmosphere of argon. The carbon is believed to partially remove the silica layer on the silicon carbide powder and thus allow matter transport. The boron is then presumed to diffuse into the silicon carbide grain boundaries and pore surfaces and promote densification.[19] The excess carbon may also inhibit exaggerated grain growth by pinning the grain boundaries.

---

*NC-203, Norton Co., Worchester, Ma.

**Hexalloy, Sohio Engineered Materials, Niagara Falls, NY

2.2 Specimen Preparation

Surfaces subject to examination were first mechanically polished. The polishing procedure began with 15 μm diamond paste on glass, reduced to 9 μm and then 6 μm: the latter on a lapping wheel. Polishing was completed with 1 μm diamond paste on a vibration polisher. Several specimens were thermally treated to highlight grain boundaries prior to examination. Treatments were conducted in vacuum or argon atmospheres. Temperatures ranged from 1300°C to 1600°C and times from 15 to 45 minutes.

2.3 Characterization Techniques

Chemical analysis was performed on both materials to determine the total boron, silicon, carbon, and oxygen contents. For boron analysis samples were crushed and the boron leached out into an acid solution. This solution was then plasma heated and the photon intensities characteristic of boron determined. The silicon content was determined by fusing powdered SiC. The resultant glass was dissolved in a hydrochloric acid solution and the silicon evaluated using atomic absorption. The carbon content was determined by fusing with an oxidant to evolve carbon dioxide. The carbon dioxide content was then analyzed using a coulometer and a carbonate standard.

Finally, the oxygen content was determined by neutron activation analysis. Other impurities were identified using semi-quantitative spectroscopic procedures.

A microprobe was used to determine the composition of second phase impurities from X-ray spectra and maps. The scanning electron microscope (SEM) was used to obtain information about porosity and carbon inclusions: the former on uncoated, mechanically polished surfaces and the latter on gold coated fracture surfaces. Transmission electron microscopy (TEM) was used to examine grain boundary phases employing both light and dark field techniques. Electron energy loss spectroscopy also identified the principal second phases.

Finally, the amounts of each SiC polytype present were determined using X-ray diffraction in conjunction with the analysis described by Rexer, et al.[20]

2.4 Material Characteristics

i. Hot-Pressed Silicon Carbide

Specimens having a light thermal etch observed in the optical microscope revealed a grain size of about 1.5 μm. The chemical analysis (Table 1) indicated appreciable oxygen, aluminum, tungsten and cobalt. The tungsten and cobalt were presumably introduced by the cobalt bonded tungsten carbide grinding media used to mix the initial powders.

Table 1

Material Composition

MATERIAL (quantitative composition)	MAJOR IMPURITIES (semi-quantitative)
Hot-Pressed SiC	1.50 wt% Al
29.84 wt% C	2.50 wt% W
64.89 wt% Si	0.10 wt% Co
50 ppm B	0.10 wt% Fe
1.70 wt% O	
Sintered α-SiC	0.18 wt% Al
30.50 wt% C	0.07 wt% Ca
69.40 wt% Si	0.06 wt% Cu
0.15 wt% B	0.16 wt% Fe
0.23 wt% O	

Microprobe analysis confirmed appreciable quantities of second phases. Backscattered electron images (Fig. 6) and related X-ray spectra identified silicides (Fig. 7) having variable composition. Some of these are tungsten silicide (dashed line) while others are a mixture of tungsten, cobalt, and iron silicides (solid line). The silicides are also revealed by TEM as intergranular second phase particles (Fig. 8). Attempts to image a grain boundary phase in the TEM were unsuccessful, indicating that amorphous phases, if present, must be less than ~5Å in width. A surface examined by SEM after a short thermal etch in argon shows large scale inhomogeneities (Fig. 9). The crack like features are presumed to be formed by volatilization of SiO formed by the reaction of SiC with Al_2O_3*, subject to low oxygen partial pressure conditions. A longer thermal etch revealed a high number density of bright-contrast second phase particles (Fig. 10) that increase in quantity with time, indicating that these phases migrate to the free surface at high temperature. X-ray analysis of these phases indicates that they are silicides having variable composition (Figs. 11a and b). Even longer thermal treatments cause the particles to assume different

---

*$SiC + Al_2O_3 \rightarrow SiO + Al_4C_3$

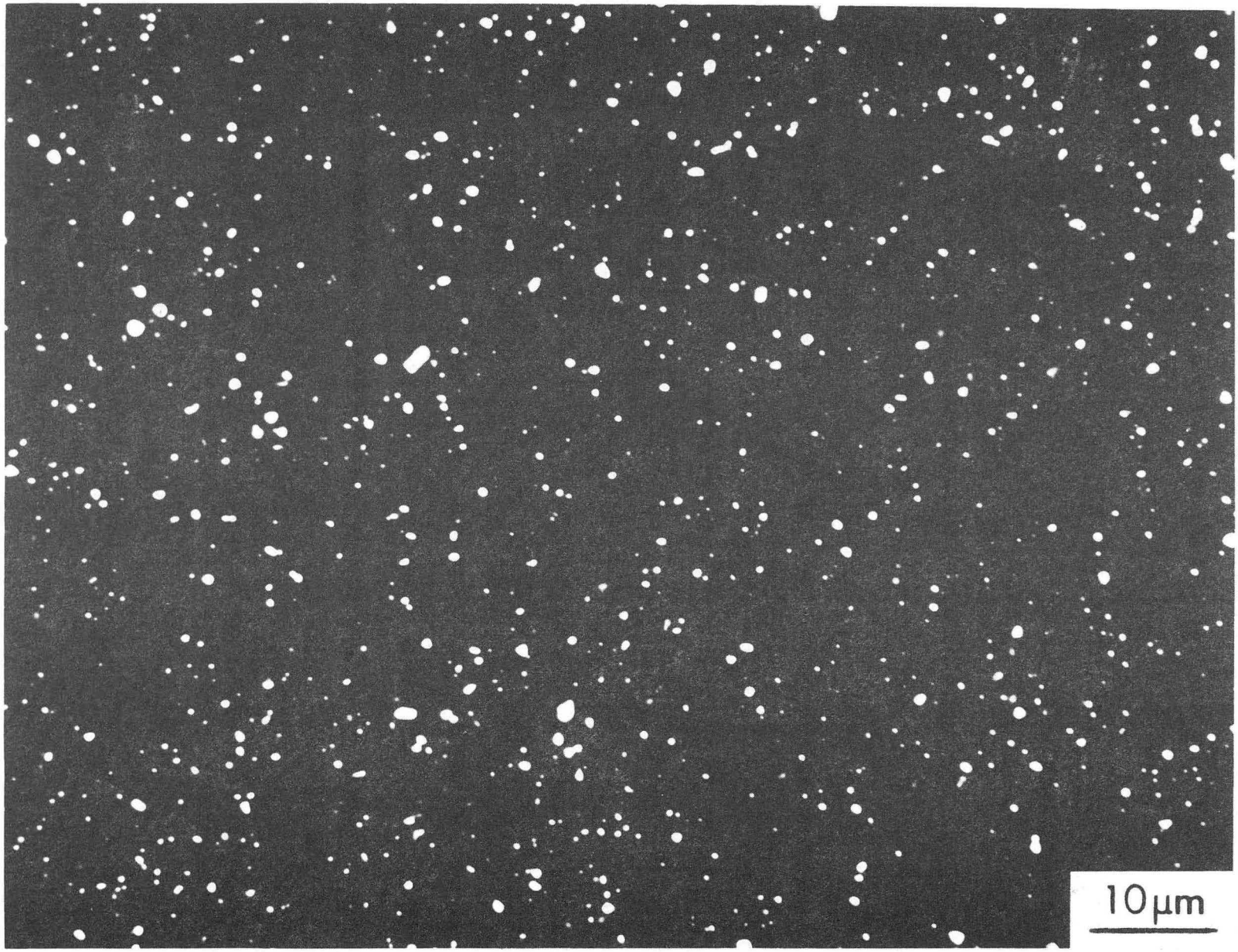

XBB 864-3127

BEI

FIG. 6

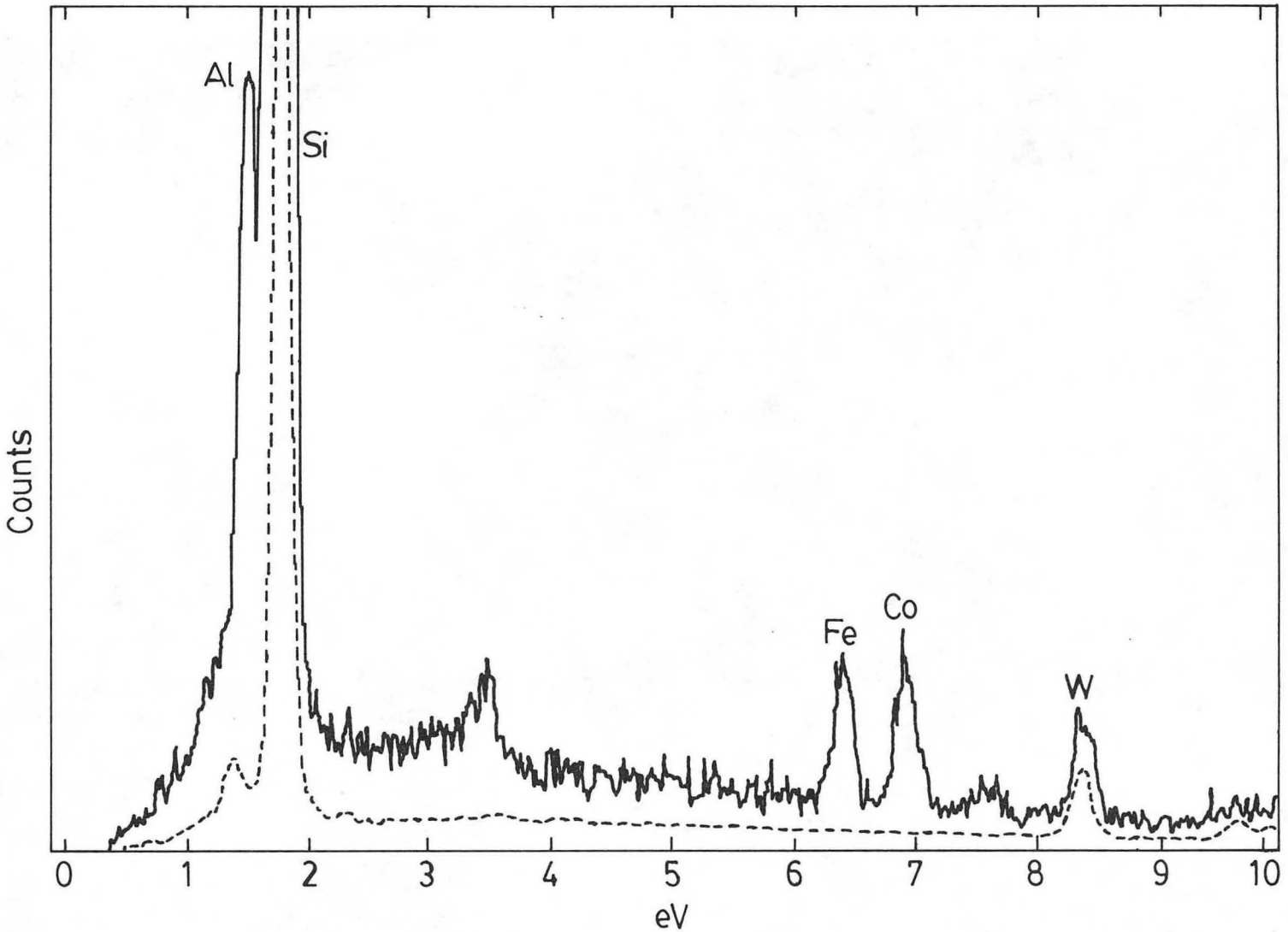

XBL 869-3245

FIG. 7

FIG. 8

XBB 864-3124

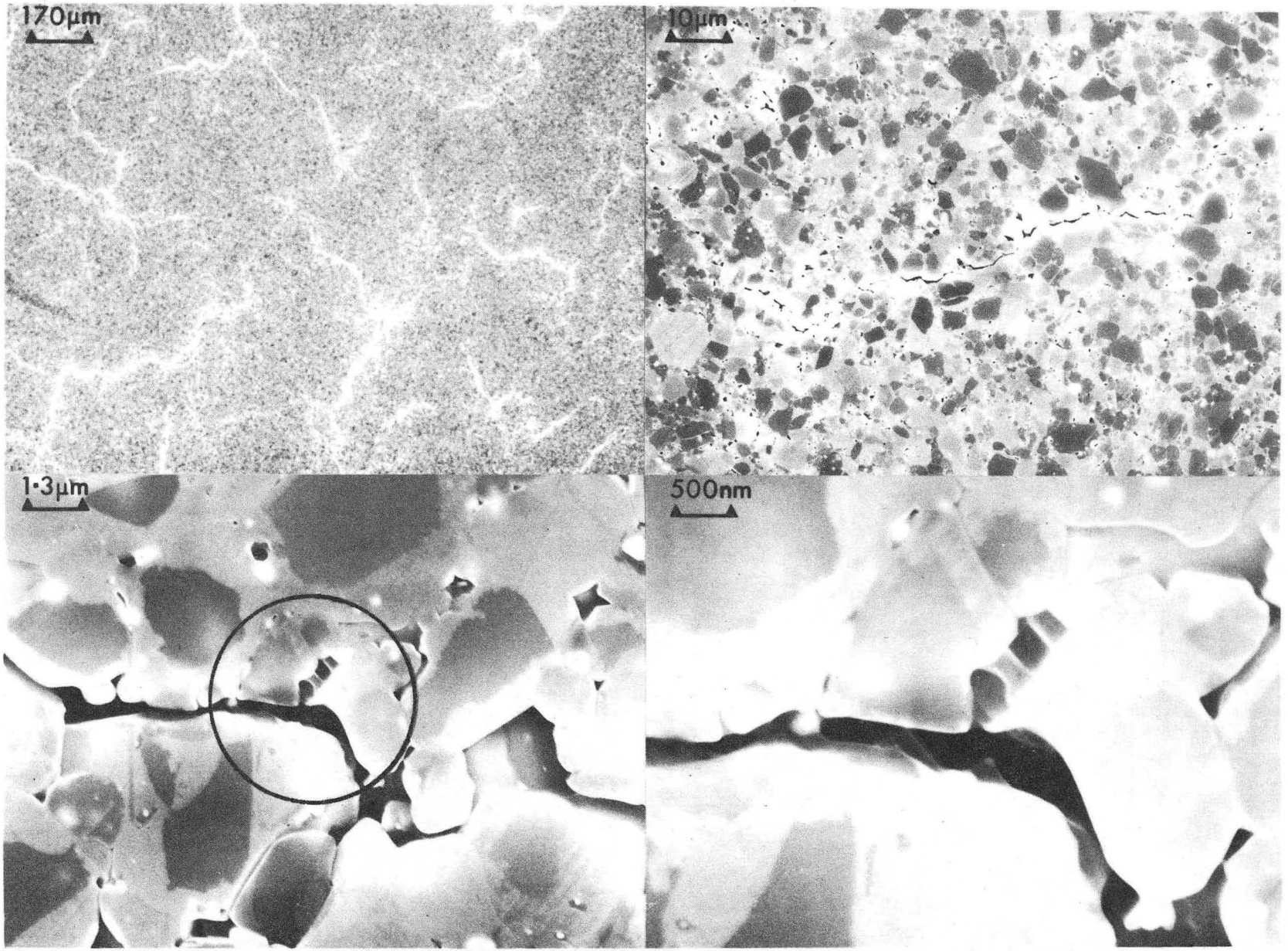

XBB 869-7494

FIG. 9

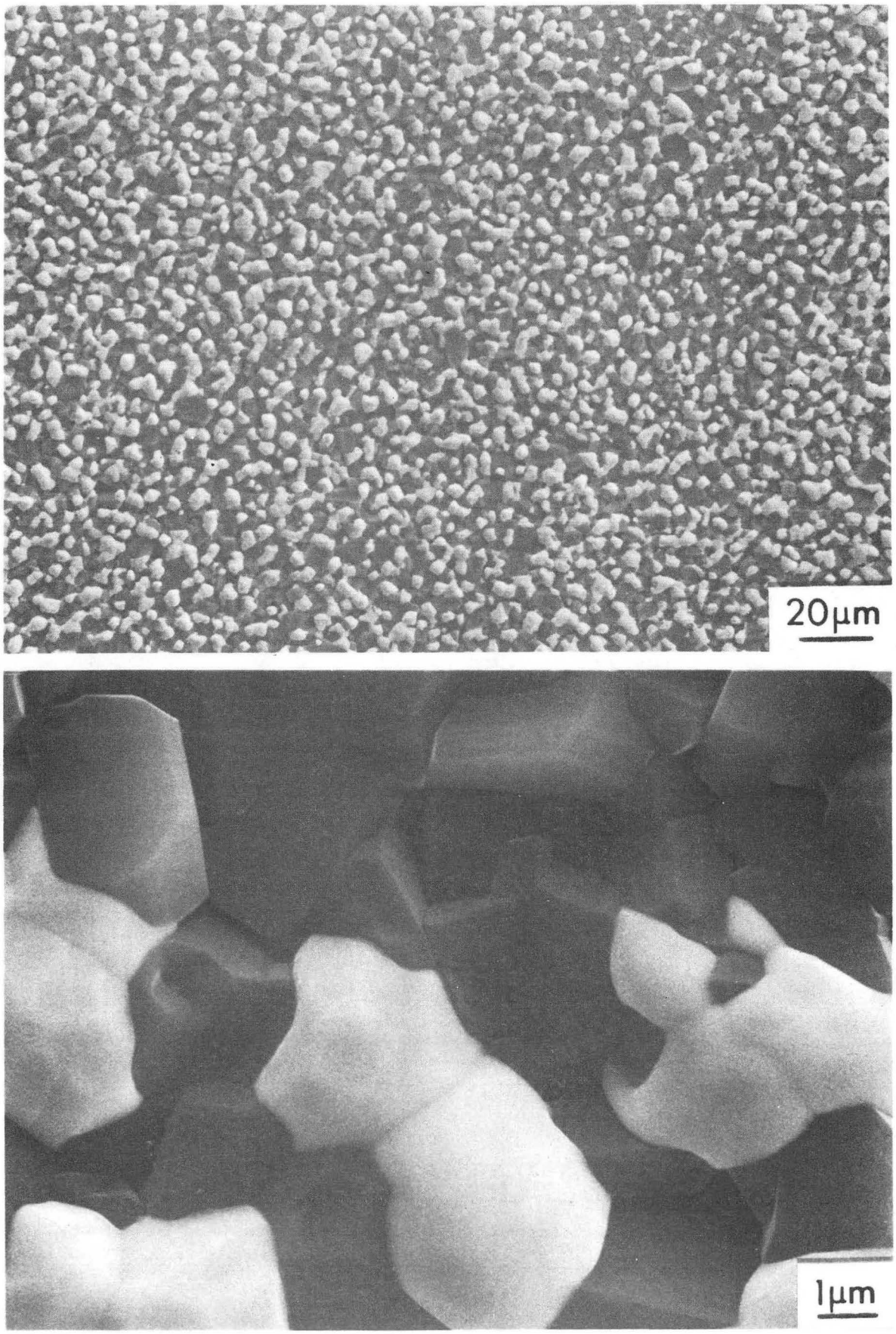

FIG. 10

XBB 864-3133

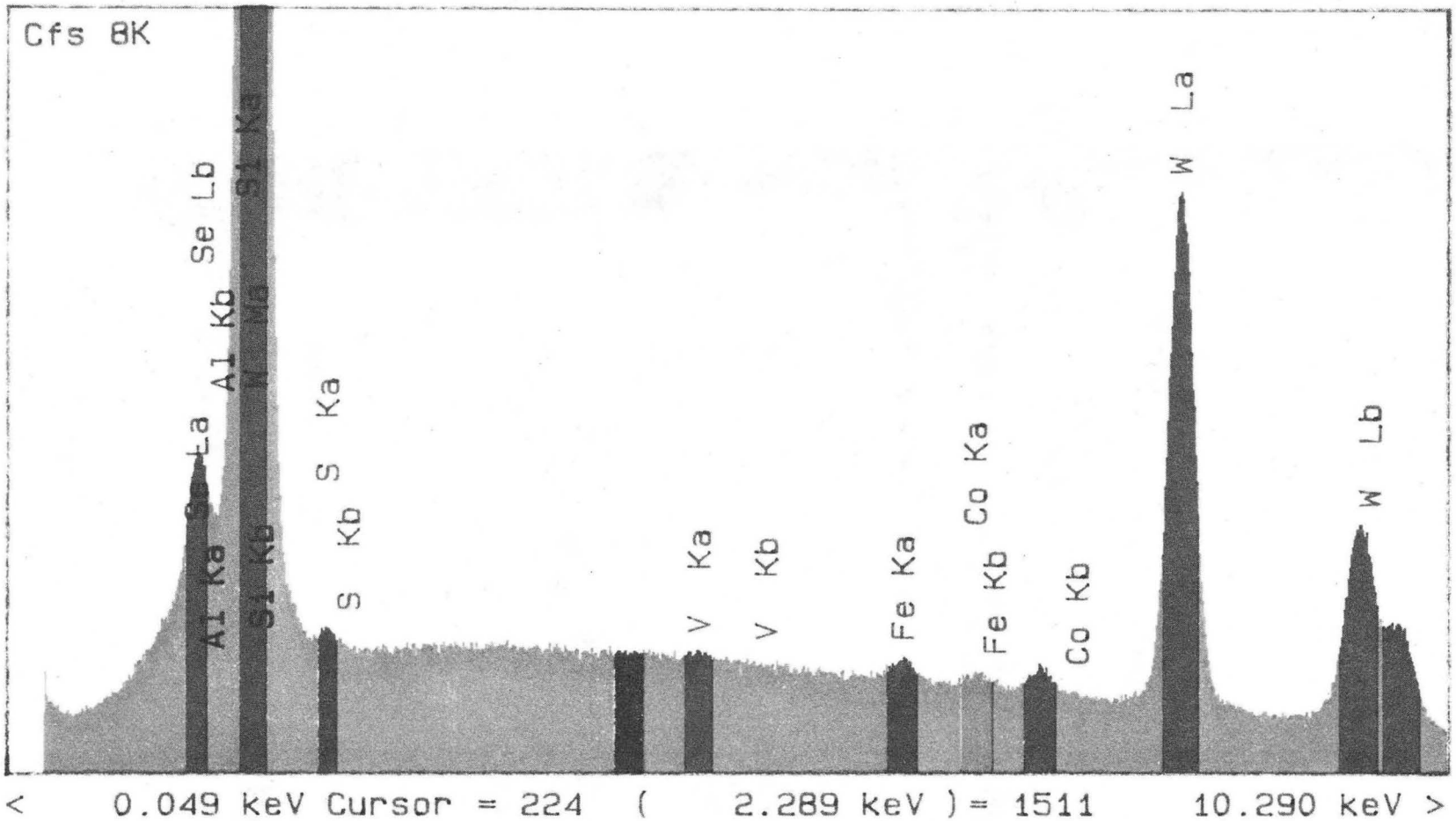

CBB 867-5925

FIG. 11a

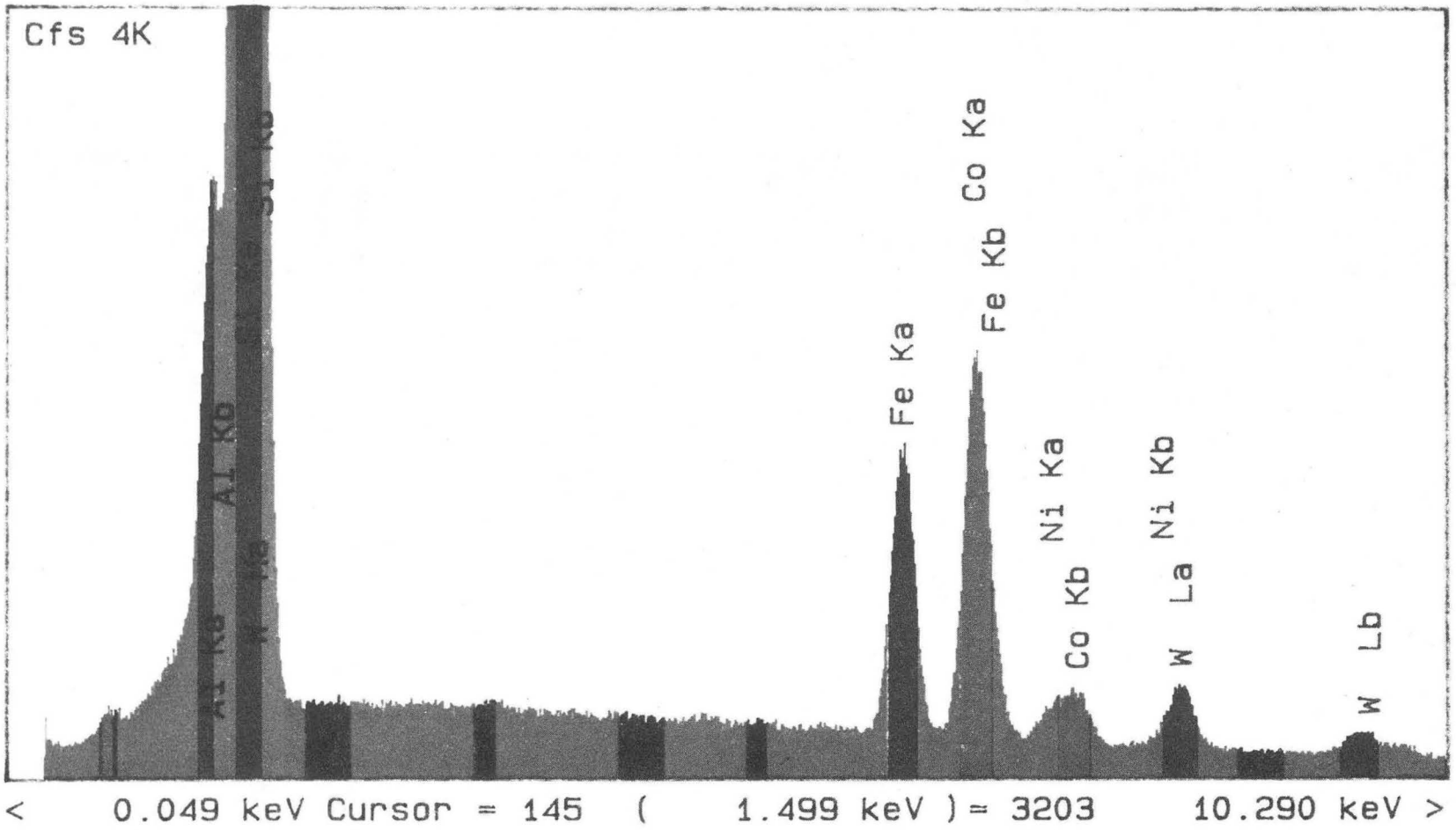

CBB 867-5921

FIG. 11b

morphologies and X-ray mapping shows compositional variations between the differently shaped particles (Fig. 12). Note that the aluminum is present everywhere while the other cations are confined to the second phase.

The X-ray diffraction data were consistent with a predominance of the 6H polytype, and detectable quantities of 15R, 4H and 3C, together comprising about 5% of the volume of the material.

ii. Sintered Silicon Carbide

Optical observations of thermally etched specimens revealed a grain size of about 10 μm. Chemical analysis (Table 1) indicated few impurities. Residual carbon is also implied by these results. Specifically, by assuming that all the silicon and boron present are in the form of carbides the residual carbon content can be estimated as 0.8 wt%. The presence of residual carbon is confirmed by transmission electron microscopy (Fig. 13a). Most definitively, the fine structure of the energy loss spectrum identifies the material as graphite (Fig. 13b). Additionally the laminar structure is consistent with the graphitic form. The graphite is present both at intergranular and intragranular sites (Fig. 14). The residual graphite is also well delineated on fracture faces (Fig. 15). Titanium and vanadium silicides have also been identified (Figs. 16, 17).

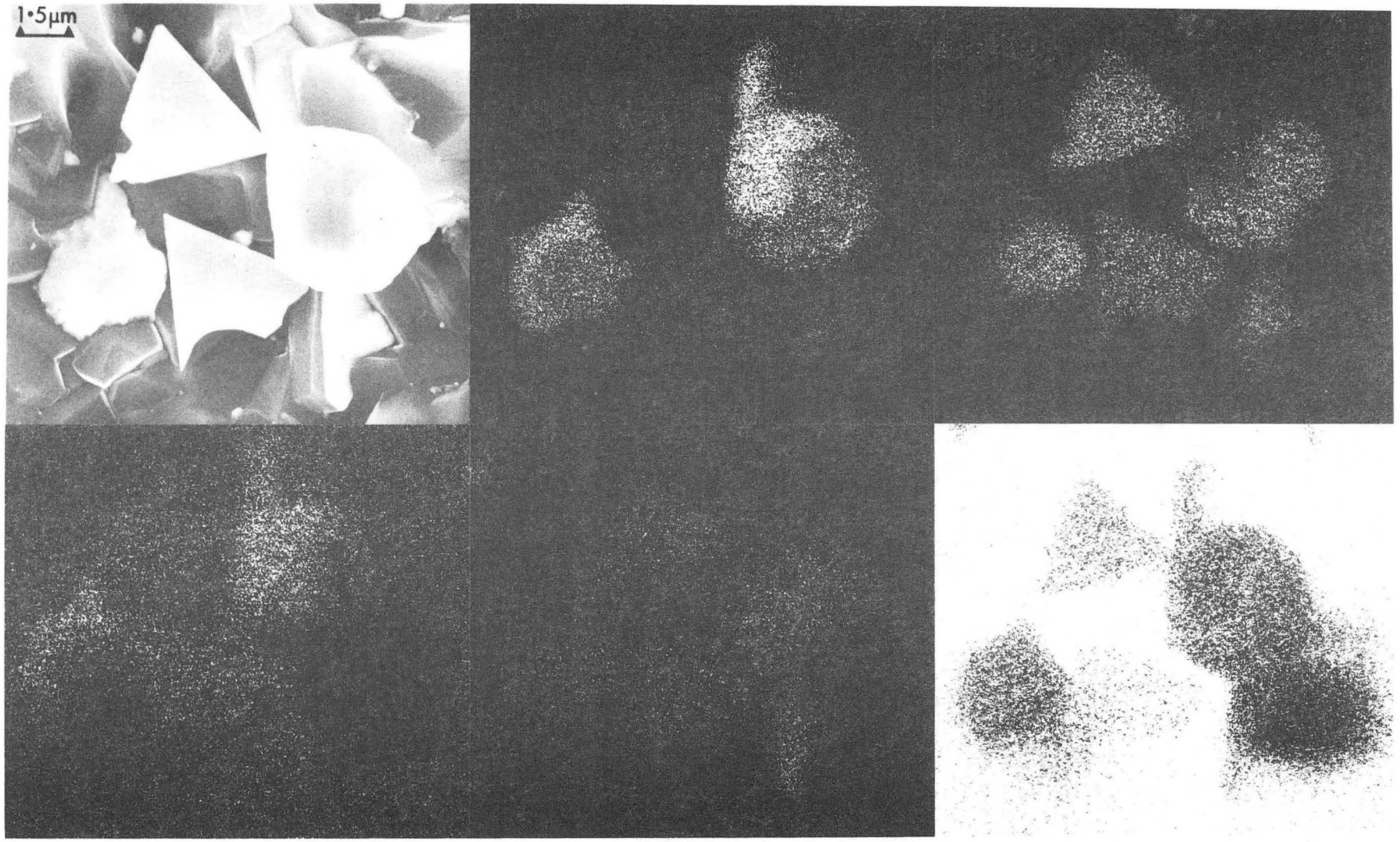

XBB 869-7067

FIG. 12

(a)

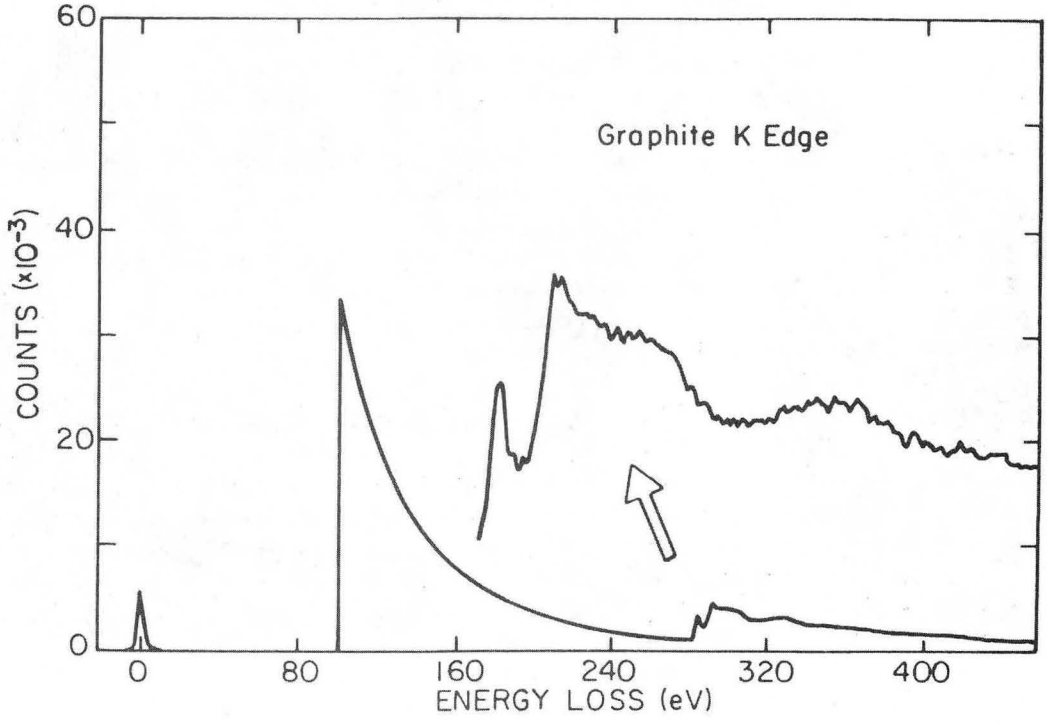

(b)

XBB 869-7069

FIG. 13

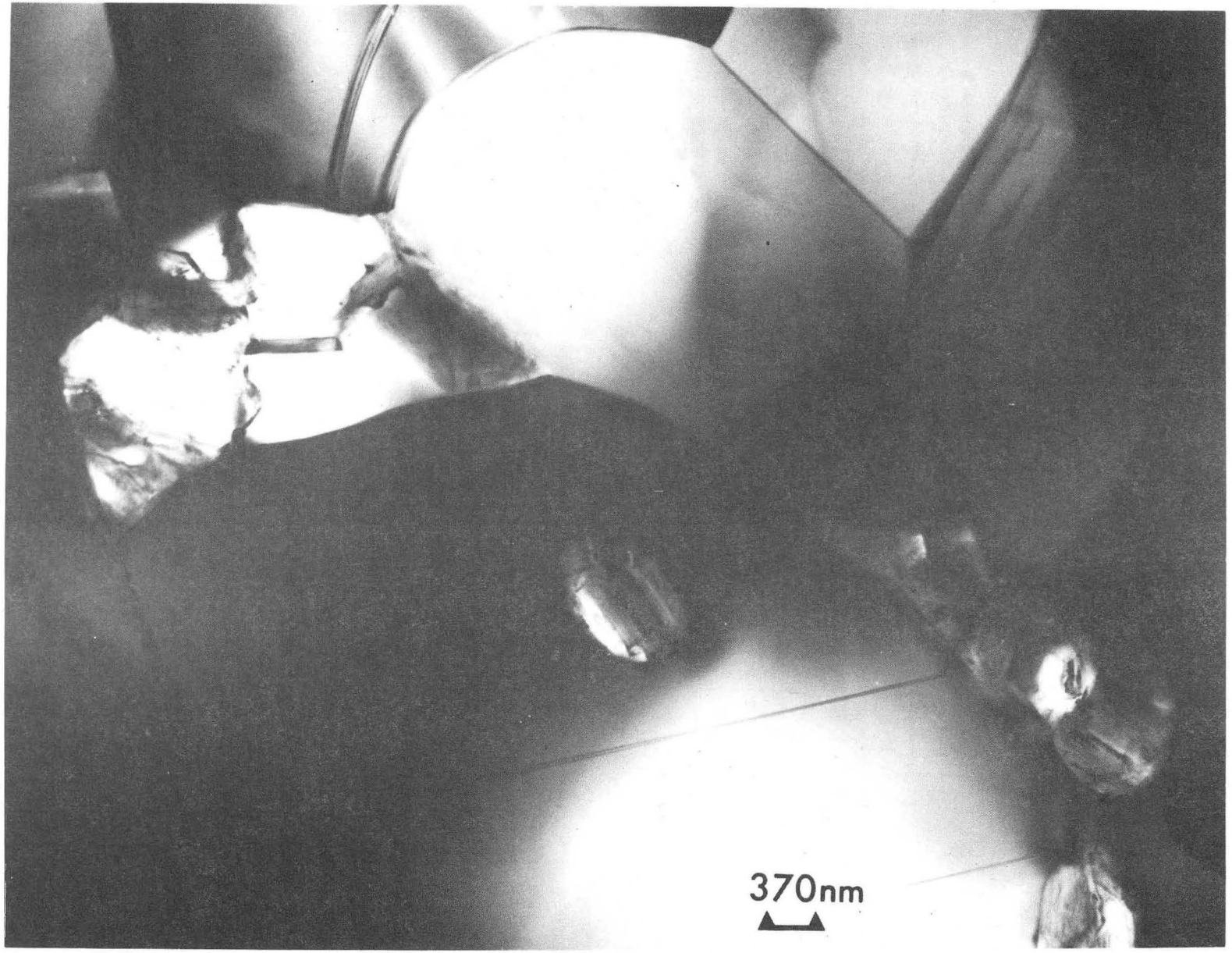

FIG 14

XBB 869-7061

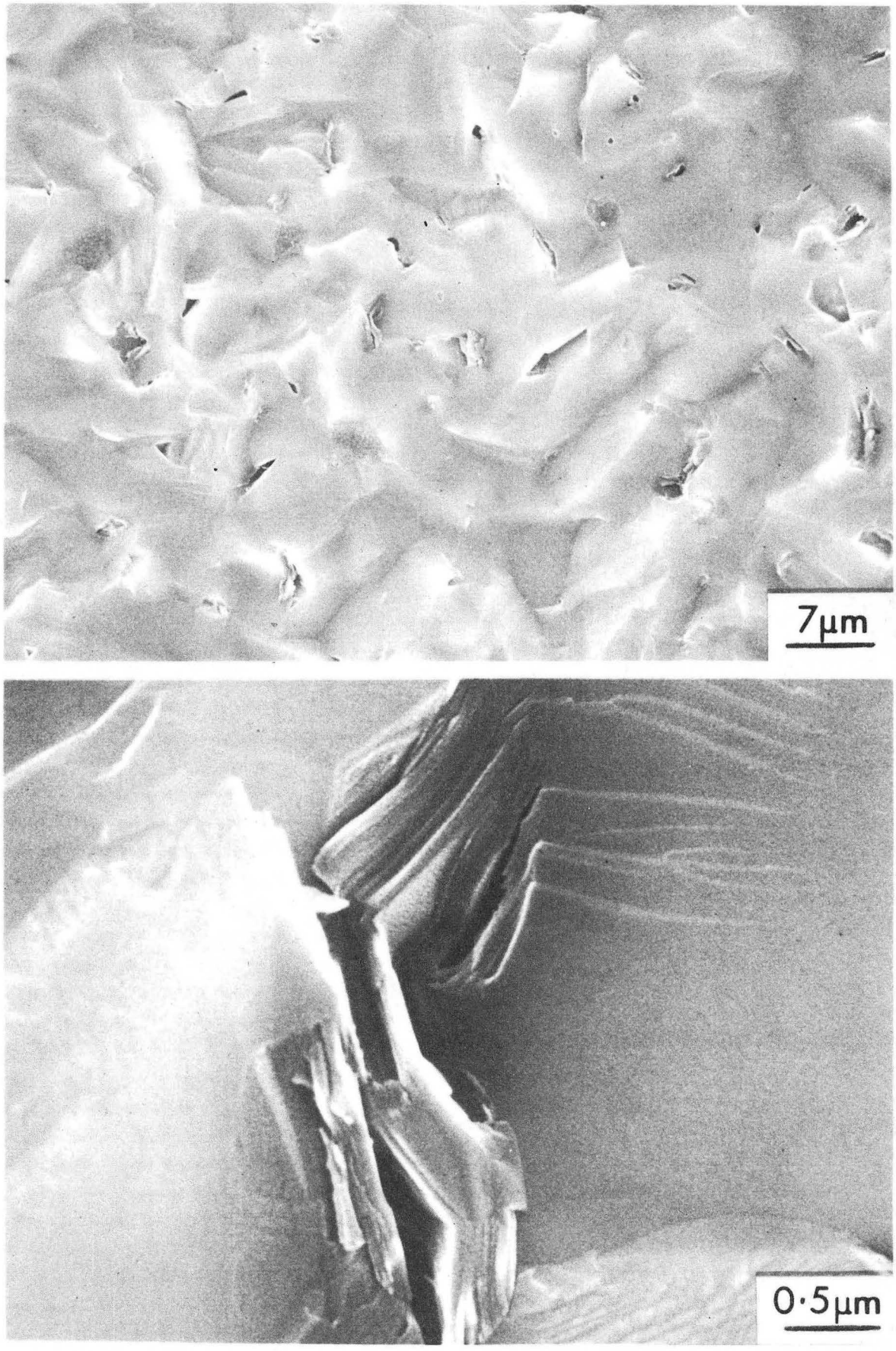

FIG. 15

XBB 864-3132

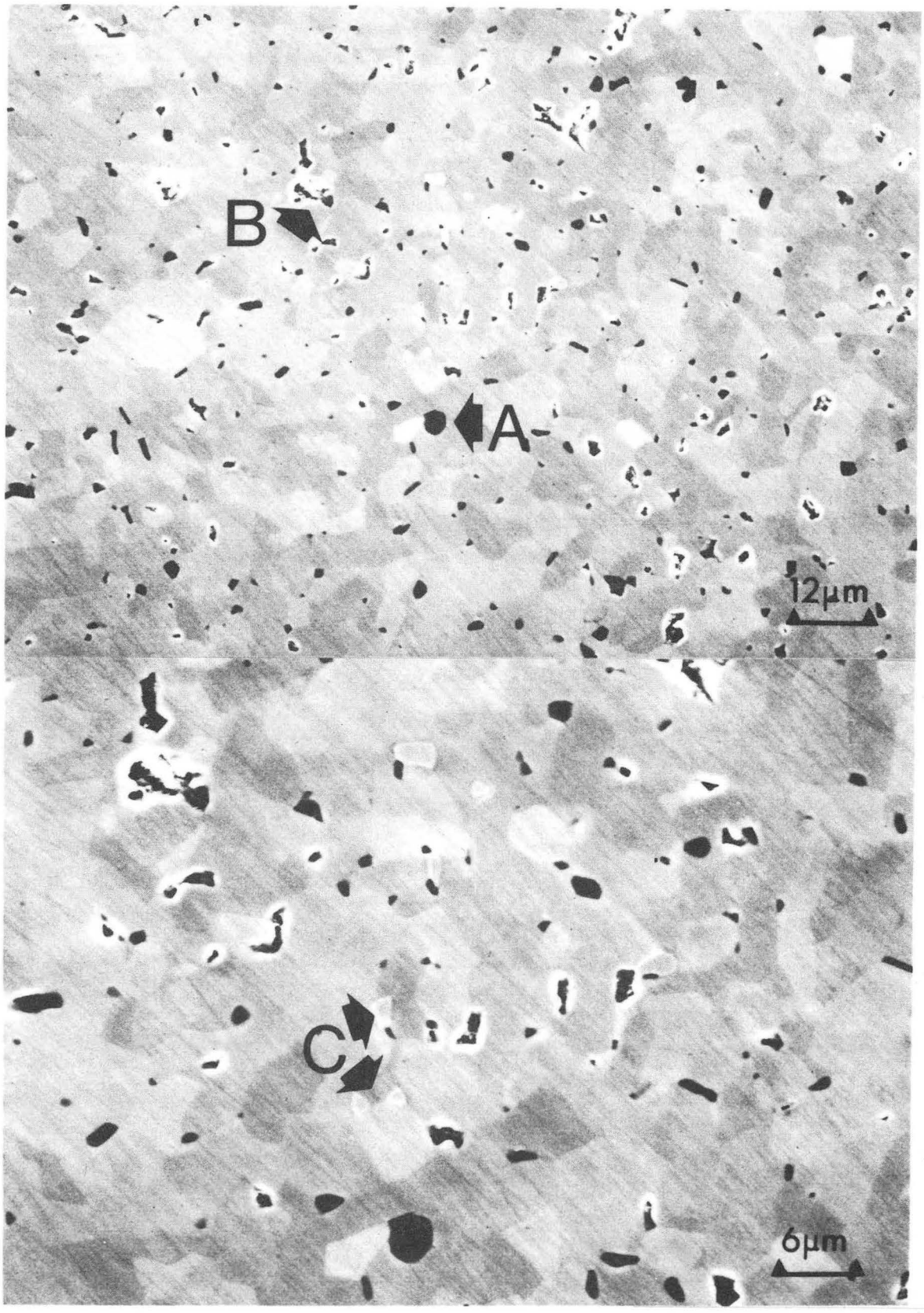

XBB 869-7065

FIG. 16

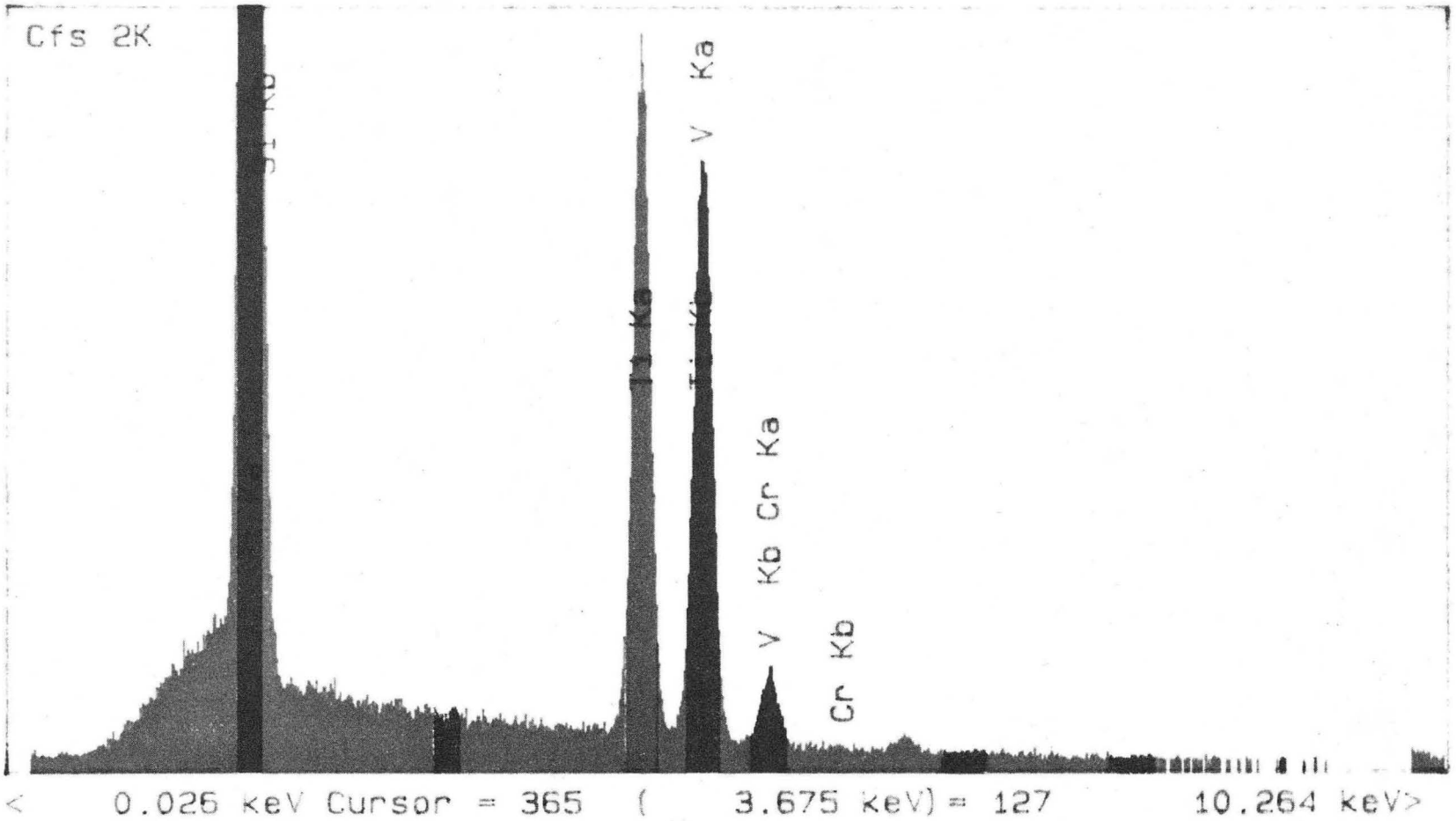

CBB 867-5923

FIG. 17

Finally, X-ray diffraction indicated mostly 6H polytype with about 5 vol% 3C and trace amounts of 15R and 4H.

3. MECHANICAL PROPERTIES

3.1 Techniques

The mechanical properties were investigated in four point flexure using 3x3x30 mm beams. Some beams were indented on the tensile surface, with a 200N Knoop indent, such that the long axis of the indenter was oriented perpendicular to the applied stress axis. The indent created a semicircular crack having 125 to 150 μm radius. The residual stress was removed by surface polishing. The edges of the tensile surface were also bevelled to remove edge flaws that might cause premature failure.

The fracture toughness was determined as a function of temperature by using indented beams tested at a strain-rate of 6×10^{-5} s^{-1}. The initial flaw size due to the indent was measured on the fracture surface in the SEM. The critical stress intensity factor, K_c, was determined with the relation[21]

$$K_c = (2/\sqrt{\pi})\ \sigma\sqrt{a} \qquad (1)$$

where σ is the applied stress and a is the initial flaw radius.

Creep tests were performed at 1600 to 1800°C in an argon atmosphere, and at constant displacement rates of 10^{-7} to 10^{-9} m/s and the steady state creep properties

characterized by[22]

$$\dot{\varepsilon} = \dot{\varepsilon}_o \left(\frac{\sigma}{\sigma_o}\right)^n \qquad (2)$$

where $\dot{\varepsilon}$ is the strain rate, σ is the stress, n is the creep exponent, and $\dot{\varepsilon}_o$ and σ_o are constants. The steady-state stress on the tensile surface was calculated using[23]

$$\sigma = \frac{3(L - \ell)P}{bh^2} \left[\frac{2n + 1}{3n}\right] \qquad (3)$$

where L is the outer span in four point bending, ℓ is the inner span, P is the load, b is the thickness, and h is the height.

Sequential testing was used in some cases, with SEM examinations conducted between each iteration. The evolution of damage on the tensile surface and the behavior of the indentation flaws were thereby observed. At the conclusion of sequential testing (at about 10% strain on the tensile surface) the beams were fractured at room temperature. The material directly in front of the crack tip was then examined for damage in the SEM and a nominal toughness ascertained using Eq. (1).

3.2 Theoretical Results

Stationary cracks in a body subject to steady-state creep generate displacement and strain fields directly analogous to the corresponding non-linear hardening solutions. Consequently the behavior of cracks in the vicinity of the brittle to ductile transition temperature can be addressed and interpreted by invoking the appropriate non-linear solutions. The relevant results are summarized in this section. For a non-linear material subject to steady-state creep (Eq. 2) the stresses outside the blunting region have the form:[24]

$$\frac{\sigma_{ij}}{\sigma_o} = \left[\frac{C^*}{\sigma_o \dot{\varepsilon}_o I r}\right]^{\frac{1}{(n+1)}} \tilde{\sigma}_{ij} \qquad (4)$$

where C* is the loading parameter, r is the distance from the crack tip, and I and $\tilde{\sigma}_{ij}$ are non-dimensional coefficients tabulated by Hutchinson.[25] At the crack tip, blunting occurs, and the stresses are locally reduced below the value predicted by Eq. (4). Within this regime, the stresses are approximately given by the stress at r = 2b (Fig. 18),[26] with b being the crack tip opening displacement that evolves during steady-state in accordance with[26]

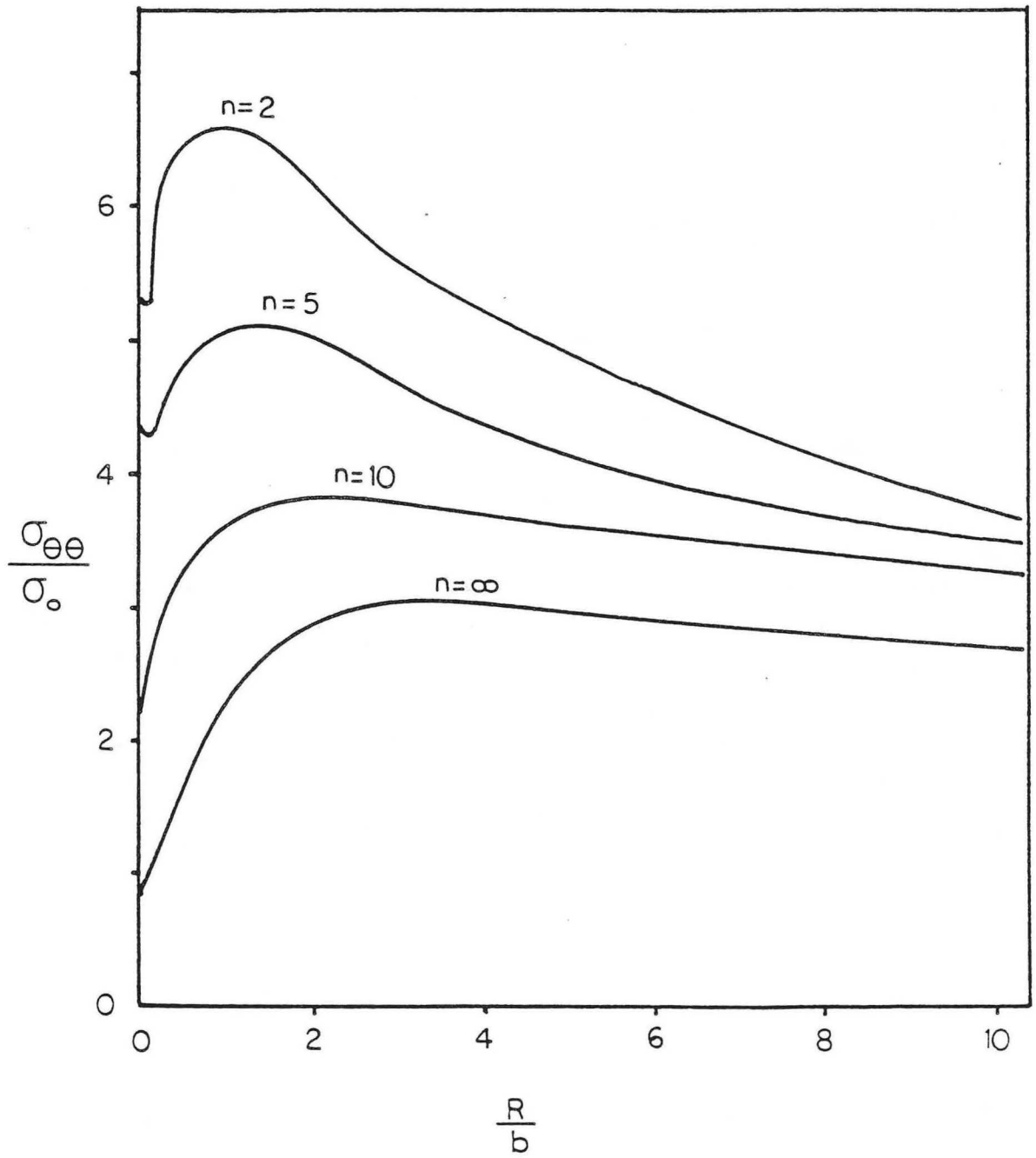
n=2
n=5
n=10
n=∞
6
4
2
0
$\frac{\sigma_{\theta\theta}}{\sigma_o}$
0
2
4
6
8
10
$\frac{R}{b}$

FIG. 18

$$\dot{b} = 0.6 \left(\frac{C^*}{\sigma_t}\right) \tag{5}$$

where σ_t is the stress at the crack tip. Hence, in steady-state

$$b = 0.6 \left(\frac{C^*}{\sigma_t}\right)\left(\frac{\varepsilon_\infty}{\dot{\varepsilon}_o}\right) \tag{6}$$

where ε_∞ is the remote strain. Rearranging Eq. (4) gives ($r \gtrsim 2b$):

$$\sigma_{ij}^{n+1} = \left(\frac{\sigma_\infty^n \, C^*}{I \, r \, \dot{\varepsilon}_\infty}\right) \tilde{\sigma}_{ij}^{n+1} \tag{7}$$

Furthermore, noting that

$$C^* = \sigma_\infty \, \dot{\varepsilon}_\infty \, a \, h_s \tag{8}$$

where h_s is a constant, gives

$$\frac{\sigma_{ij}}{\sigma_\infty} = \left[\frac{h_s a}{I \, r}\right]^{\frac{1}{(n+1)}} \tilde{\sigma}_{ij} \qquad (r \gtrsim 2b)$$

$$\tag{9}$$

$$\frac{\sigma_{ij}}{\sigma_\infty} = \left[\frac{h_s a}{2Ib}\right]^{\frac{1}{(n+1)}} \tilde{\sigma}_{ij} \qquad (r \gtrsim 2b)$$

The σ_{yy} stress in the crack plane predicted by Eqs. (9) is plotted in Fig. 19 for n=2 (typical of the present experiments), whereupon $h_s = 1.4$, $I = 5.8$, and $\tilde{\sigma}_{ij} = 1.8$.

When test specimens are cooled under load, the stresses given by Eqs. (9) remain. Hence, when the load is removed at room temperature, residual stresses develop. Load removal is an elastic process, whereupon the unloading stresses close to the tip are:

$$\frac{\sigma_{yy}}{\sigma_\infty} \approx - \left(\frac{2a}{b+2r}\right)^{\frac{1}{2}} \qquad (10)$$

Such that the residual stress σ^R_{yy} at the near tip for n=2 ($r < 2b$) is:

$$\sigma^R_{yy} = \sigma^C_\infty \left[.89 \left(\frac{a}{b}\right)^{1/3} - \left(\frac{2a}{b+2r}\right)^{\frac{1}{2}}\right] \qquad (11)$$

where σ^C_∞ is now the remote stress on the body during creep and upon cooling.

Conduct of a room temperature fracture test on specimens cooled under load is governed by superposition of the new elastic field upon the residual field. At fracture, when $\sigma^\infty \equiv S$, the stresses near the tip are then

$$\sigma_{yy} = (S - \sigma^C_\infty)\left(\frac{2a}{b+2r}\right)^{\frac{1}{2}} + .89\, \sigma^C_\infty \left(\frac{a}{b}\right)^{1/3} \qquad (12)$$

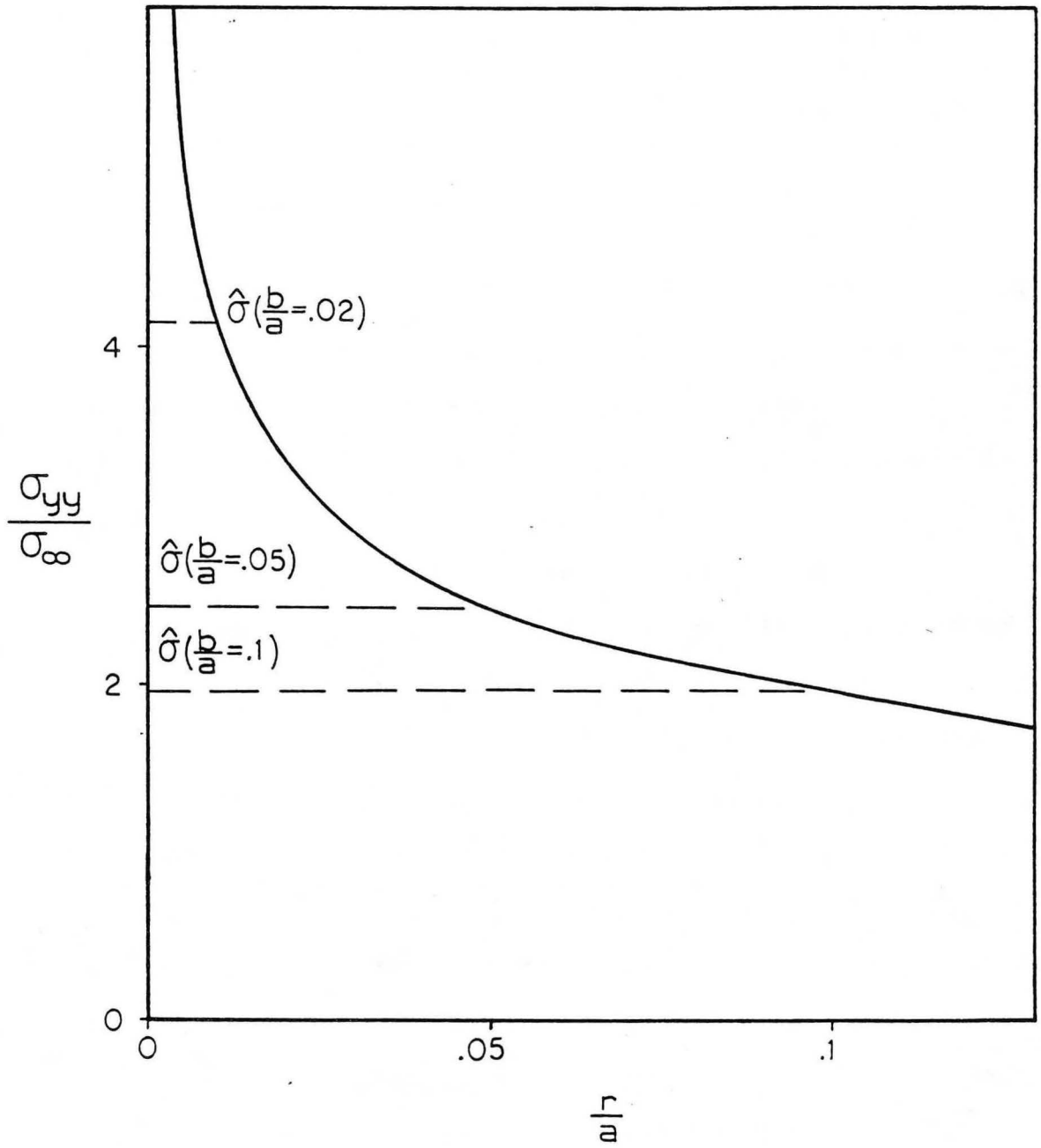
$\hat{\sigma}(\frac{b}{a}=.02)$
$\hat{\sigma}(\frac{b}{a}=.05)$
$\hat{\sigma}(\frac{b}{a}=.1)$
4
2
0
$\frac{\sigma_{yy}}{\sigma_\infty}$
0
.05
.1
$\frac{r}{a}$

FIG. 19

The fracture process may be analyzed on the basis of the stress field.

3.3 Properties

The results of the fracture toughness tests (Table 2) show that K_{Ic} is temperature insensitive in the sintered material. The hot-pressed material has a somewhat higher room temperature toughness than the sintered material, but the toughness diminishes at higher temperature to a level comparable to that of the sintered material. Specimens tested at room temperature after exposure to steady-state at high temperature gave nominal toughnesses larger than the sharp-crack toughness, as indicated in Table 2.

The creep testing revealed an abrupt transition from brittle to ductile behavior (Figs. 20 and 21, Tables 3a and b) such that, in the ductile region, the strain on the tensile surface exceeded 10% without failure. At strain-rates of $\sim 10^{-7}$ s^{-1} the transition for the hot-pressed material occurred between 1650 and 1700°C, and for the sintered material between 1750 and 1800°C. In the ductile range the creep exponent of the hot pressed silicon carbide was 2.3 and for the sintered silicon carbide 1.7. These values are in the range expected for superplastic behavior,[27] consistent with the extensive ductility observed above the transition temperature.

Table 2

Fracture Toughness of SiC as a function of Temperature

Sintered SiC	Test #1	Test #2
Room temperature	2.7 Mpa√m	2.7 MPa√m
1500°C	2.7	
1600°C	2.7	3.0
1700°C	2.9	2.6
1800°C	2.7	2.8
Hot-Pressed SiC		
Room Temperature	3.9	4.0
1400°C	2.8	
1500°C	2.7	2.6
1600°C	2.4	2.6
1700°C	2.6	2.4

Room Tempeature Tests of Deformed Beams

Specimen	Nominal Toughness
NC11	5.0
C11	5.5
C12	6.0

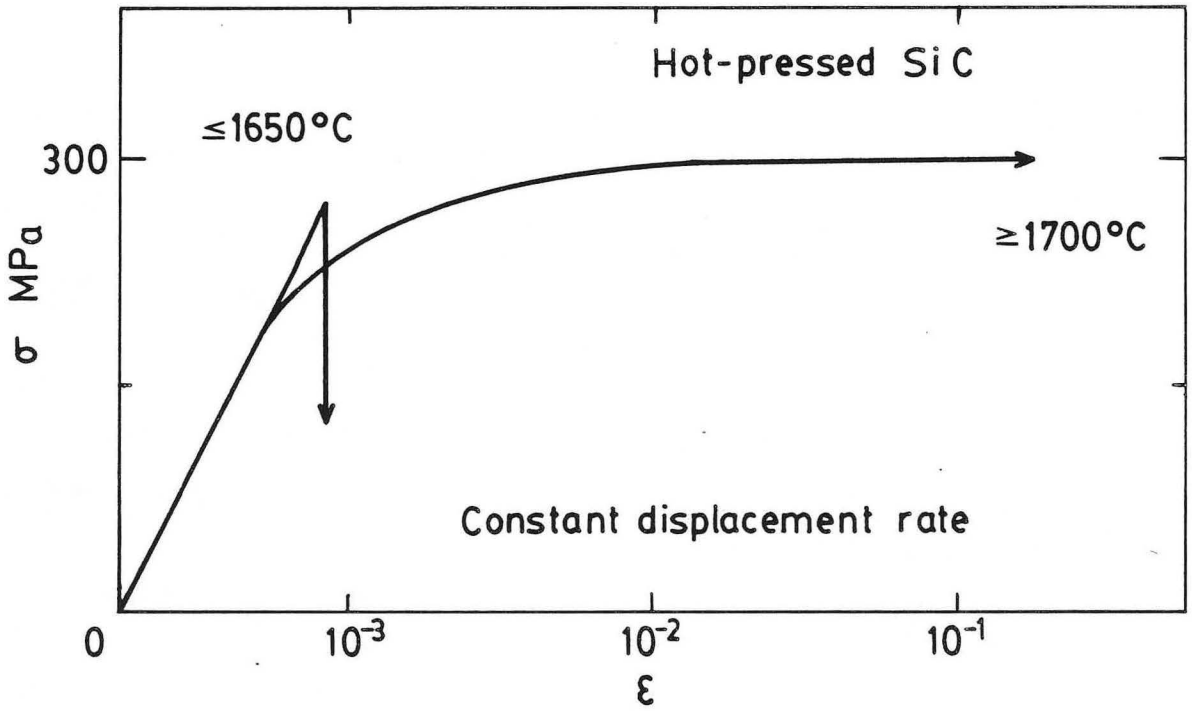

XBL 869-3240

FIG. 20

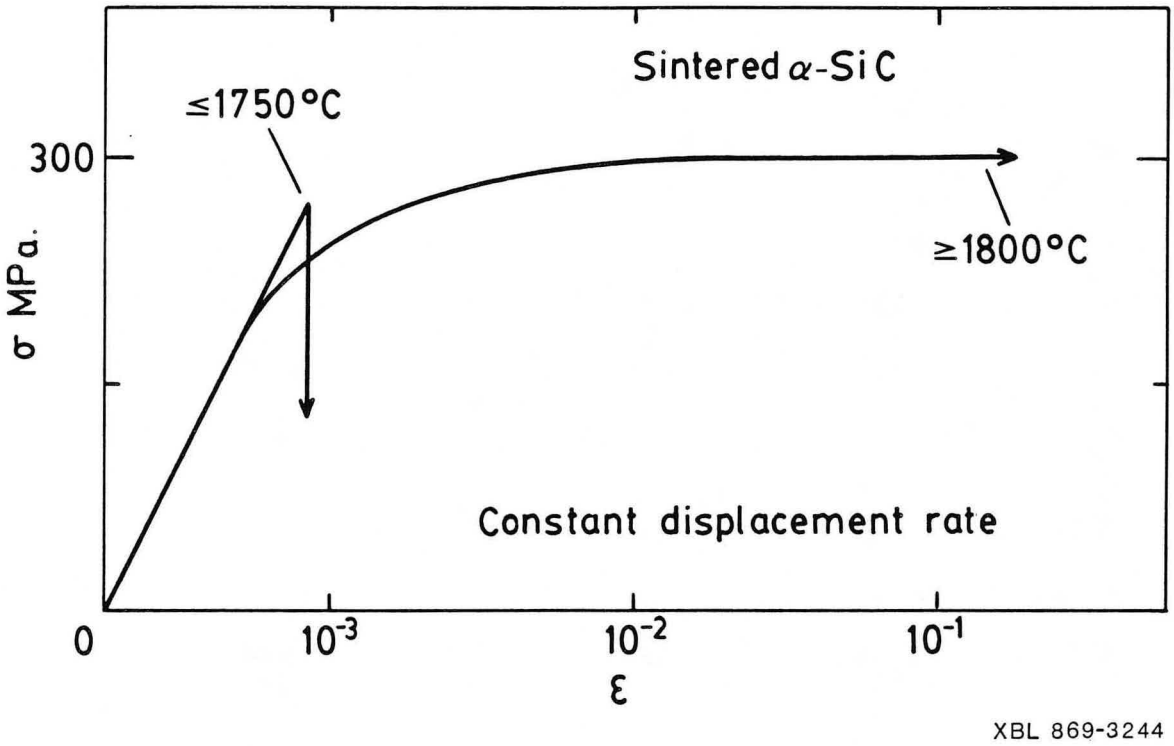
Sintered α-SiC
≤1750°C
300
σ MPa.
≥1800°C
Constant displacement rate
0
10⁻³
10⁻²
10⁻¹
ε
XBL 869-3244

FIG. 21

Table 3a

HOT-PRESSED SiC (NC203)

Specimen	Temp (°C)	Strain Rate (sec^{-1})	Total Strain	Mode	Stress (MPa)
NC2	1600	$6.8x10^{-7}$		Fracture	199
NC3	1600	$3.4x10^{-7}$		Fracture	184
NC5	1600	$1.7x10^{-7}$		Fracture	414
NC7	1600	$6.8x10^{-8}$		Fracture	252
NC7	1650	$1.7x10^{-7}$		Fracture	127
NC8	1650	$1.7x10^{-7}$		Fracture	334
NC4	1700	$1.7x10^{-7}$	5%	Flow	250
NC9	1700	$1.7x10^{-7}$	6%	Flow	235
NC16	1750	$9.5x10^{-7}$	3%	Flow	253
NC16	1750	$9.5x10^{-7}$	6%	Flow	245
Indented Beams					
NC10	1700	$1.7x10^{-7}$	3%	Flow	215
NC11	1700	$2.2x10^{-7}$	5%	Flow	310
NC11	1700	$2.2x10^{-7}$	10%	Flow	310
NC12	1700	$2.2x10^{-7}$	1%	Fracture	305
NC13	1750	$4.8x10^{-6}$	2%	Fracture	195
NC14	1750	$9.5x10^{-7}$	6%	Flow	160
NC15	1750	$9.5x10^{-7}$	3%	Flow	200

Table 3b

SINTERED α-SiC (Carborundum)

Specimen	Temp (°C)	Strain Rate (sec^{-1})	Total Strain	Mode	Stress (MPa)
C6	1700	$1.6x10^{-7}$		Fracture	262
C7	1750	$1.6x10^{-7}$		Fracture	190
C8	1800	$1.6x10^{-7}$	4%	Flow	173
C9	1800	$3.2x10^{-7}$	3%	Flow	225
C9	1800	$3.2x10^{-7}$	6%	Flow	250
C10	1750	$1.6x10^{-7}$		Fracture	208
Indented Beams					
C11	1800	$3.2x10^{-7}$	3.5%	Flow	180
C11	1800	$3.2x10^{-7}$	6%	Flow	185
C11	1800	$3.2x10^{-7}$	8.5%	Flow	190
C12	1800	$4.3x10^{-7}$	4%	Flow	228
C12	1800	$4.3x10^{-7}$	6%	Flow	230

Indentation cracks above the transition temperature in the sintered material exhibited blunting and opening without growth (Fig. 22). Furthermore, the only damage evident in the material occurred in the vicinity of the blunt tip in the form of cavities that seemingly initiated at graphite inclusions (Fig. 23). In the hot-pressed material, the behavior above the transition temperature had some differing features. In particular, some crack growth occurred (Fig. 24) albeit at a low crack growth rates. For example, the crack velocity was $\sim 10^{-9}$ m/s at values of the crack driving force $C^* \approx .013$ N/ms. viz at a nominal $K \approx 5.5$ MPa $\sqrt{m}$. Appreciable damage was also detected in a crack tip zone (Fig. 25) consisting of lenticular shaped facet cavities typical of those apparent during creep crack growth.[28]

4. DISCUSSION

The brittle to ductile transition in ceramics involves local competition between flow and fracture. At this simplest level, flow at elevated temperature is governed by steady-state creep and fracture involves the brittle propagation of an initial crack. For nominally single phase SiC materials, brittle fracture from a sharp crack is expected to be a temperature insensitive process, as affirmed by the fracture toughness measurements

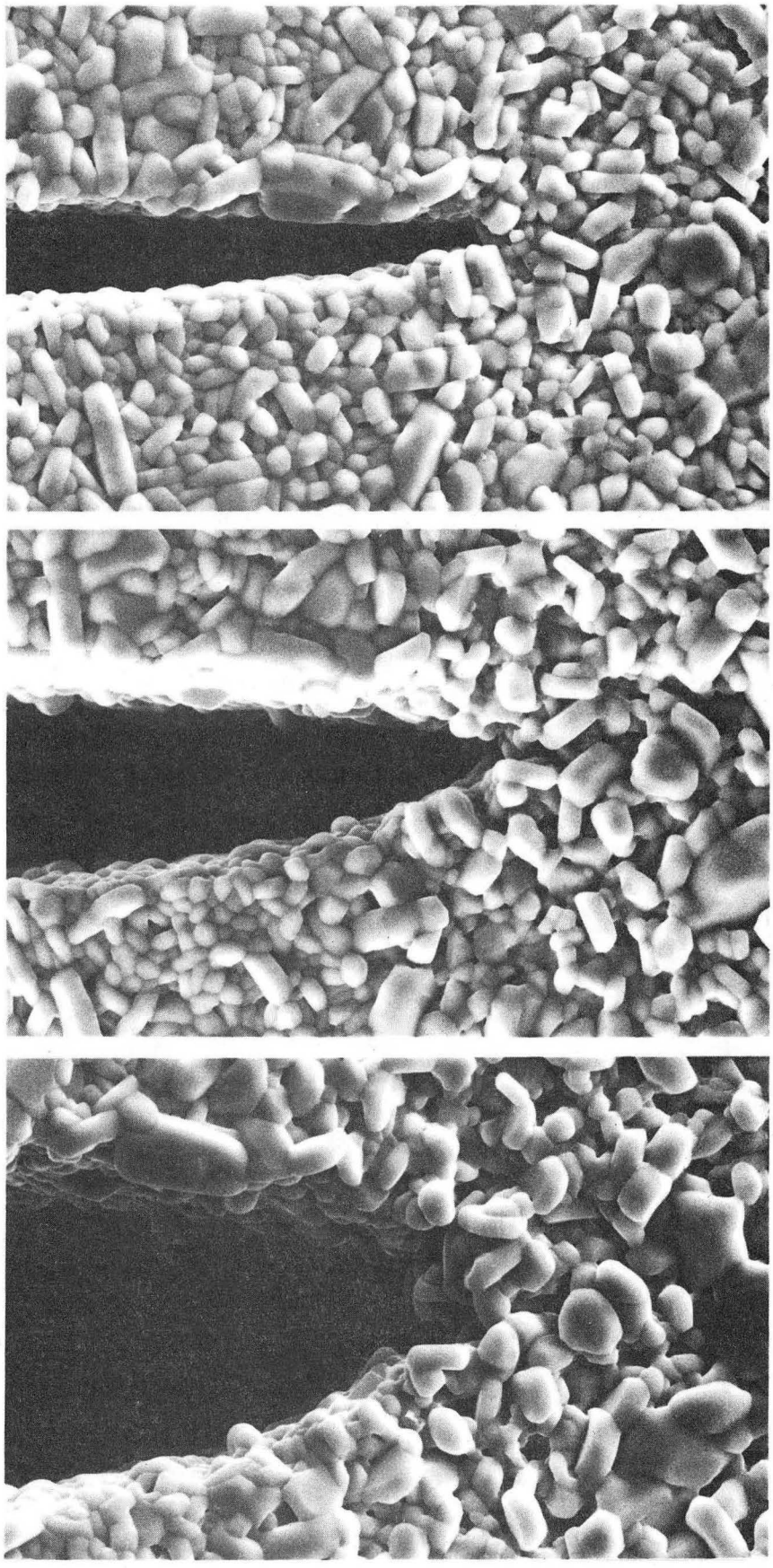

FIG. 22 XBB 865-3575

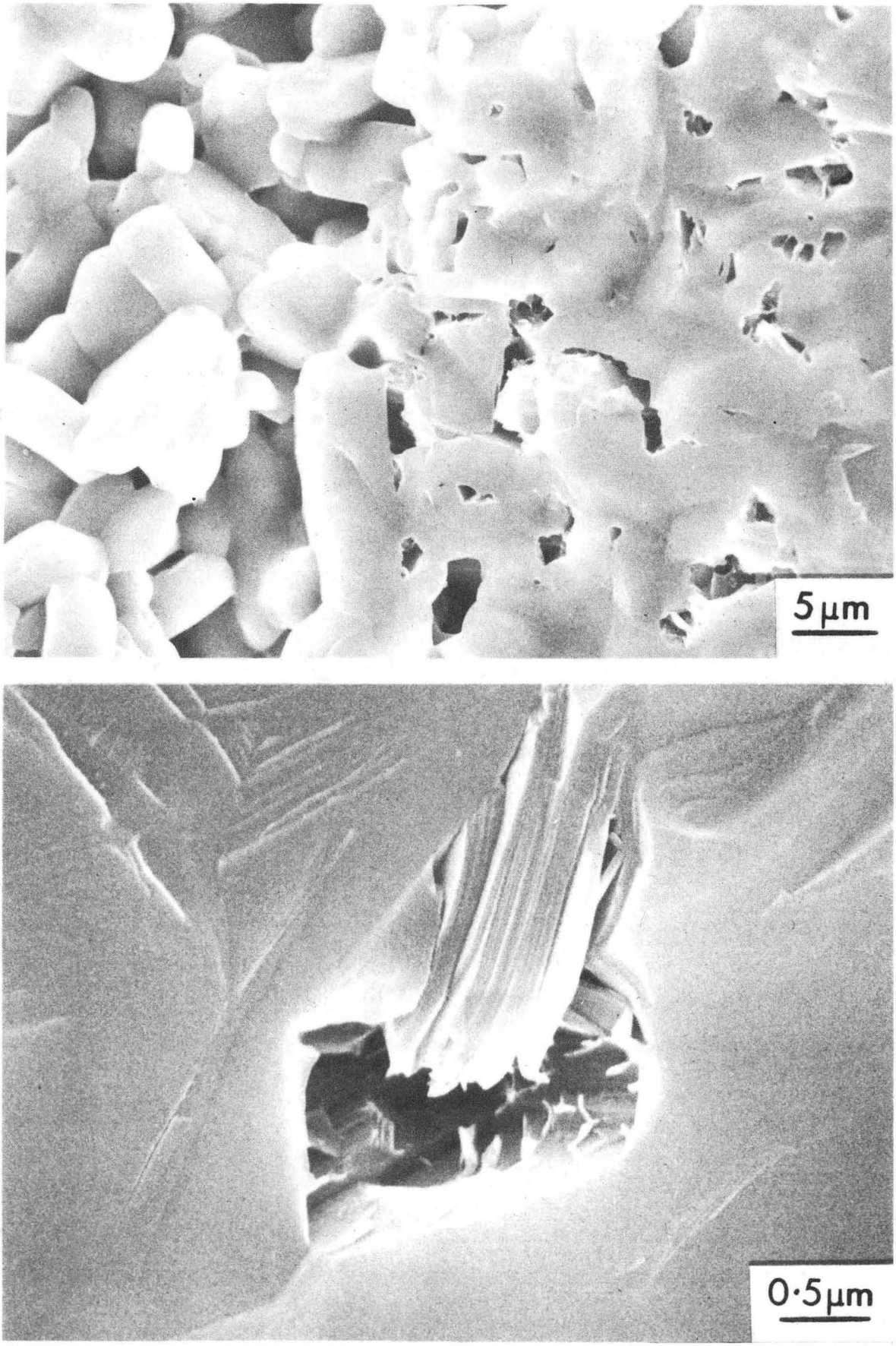

FIG 23

XBB 864-3134

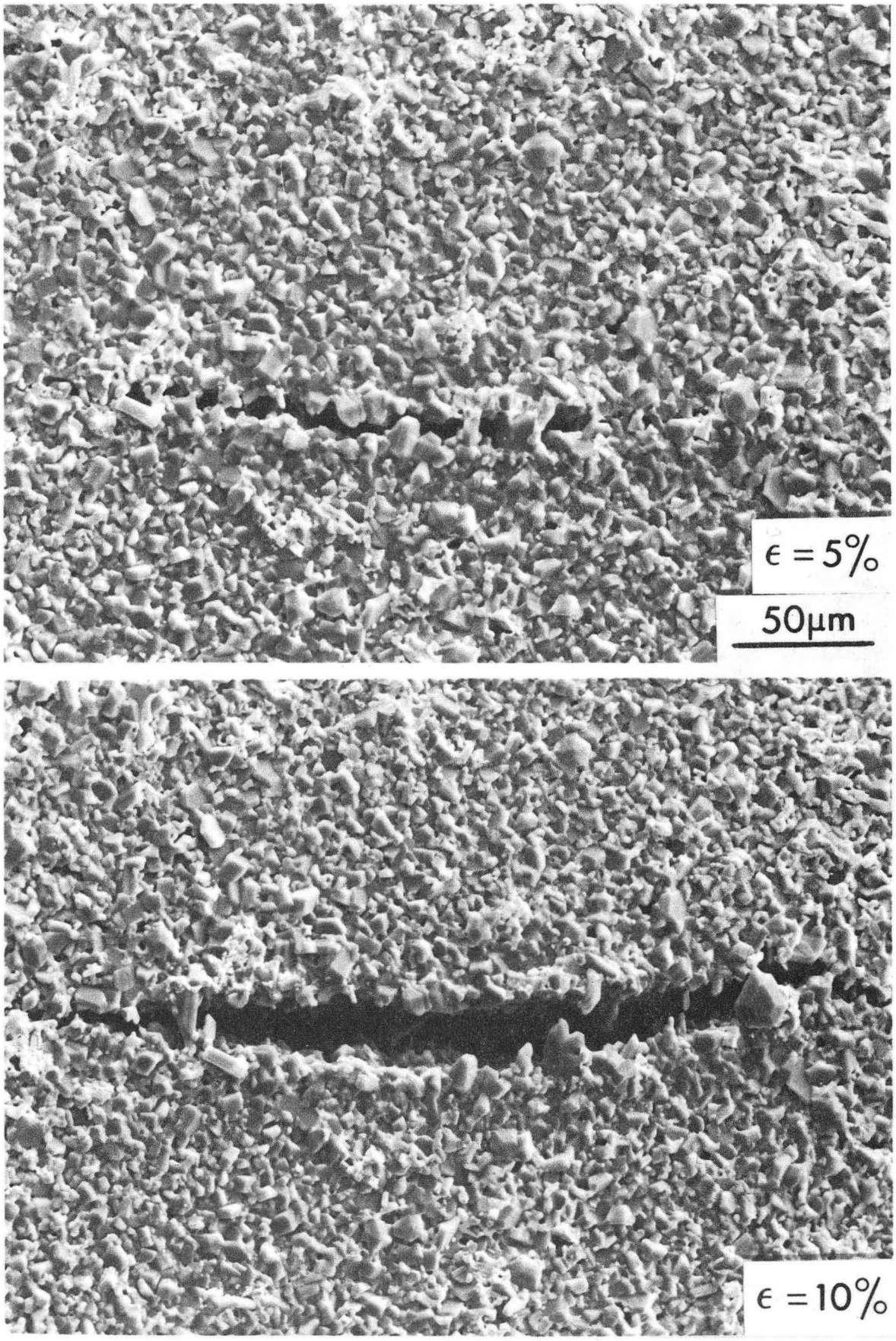

FIG. 24

XBB 864-3131

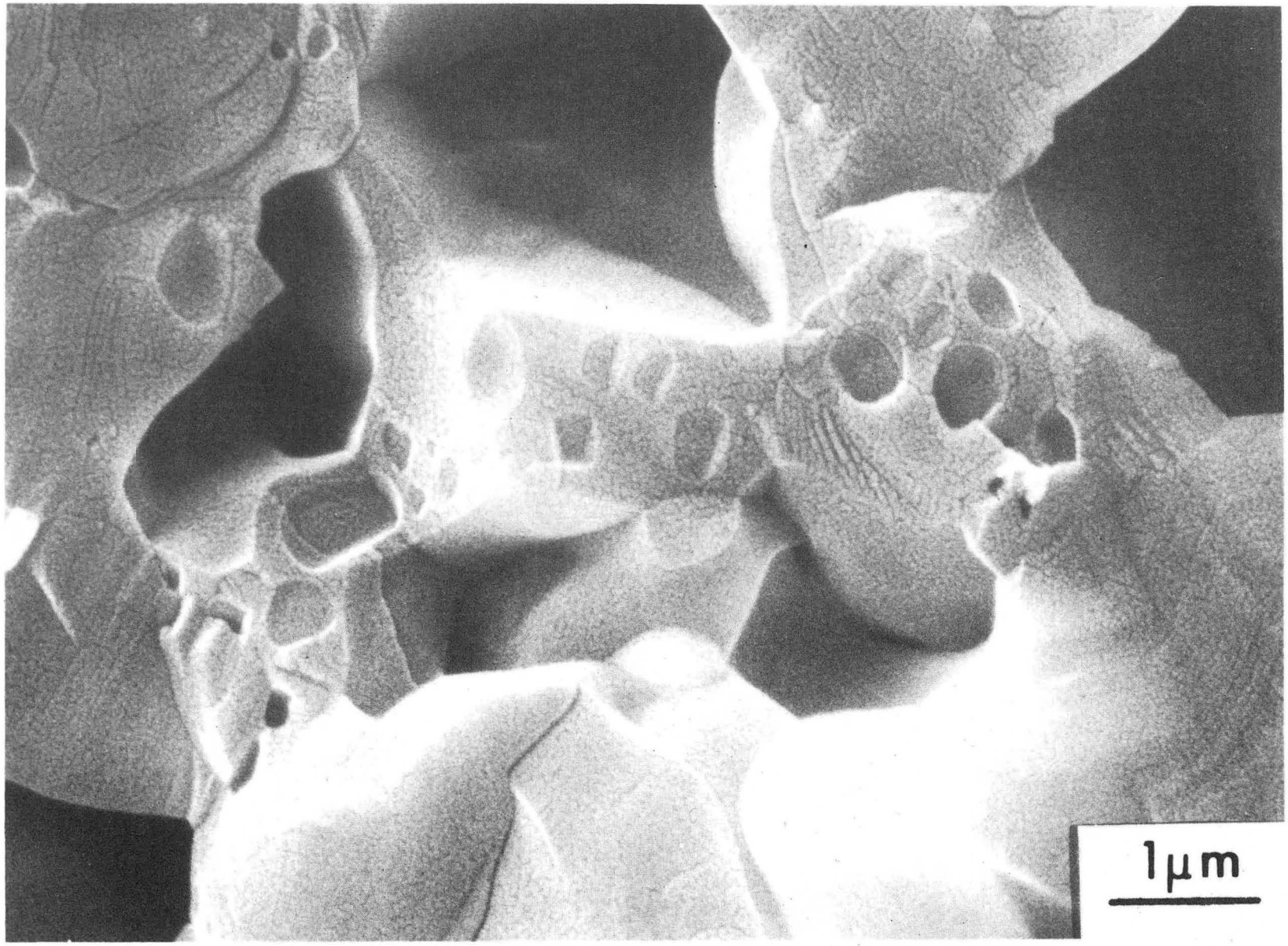

XBB 864-3122

FIG. 25

(Table 2). Consequently, the 'brittle strength' of the materials is also temperature insensitive, as plotted on Figs. 26 and 27. Conversely, deformation is strongly temperature dependent, as governed by the creep process (Figs. 26 and 27). A transition from brittle to ductile behavior would be expected to occur when the flow stress becomes smaller than the fracture stress. However, the process must occur everywhere in the body. The most critical region is clearly within the crack tip field (see Figs. 18 and 19). Further discussion thus involves consideration of the competing deformation and fracture processes near the crack tip.

4.1 The Flow Stress

The creep process in both materials exhibits characteristics typical of superplasticity: notably a stress exponent, $n \simeq 2$, and an activation energy comparable to that for grain boundary diffusion. The creep law thus has the form;

$$\dot{\varepsilon}/D_b \simeq (\sigma^2 \, \Omega^{1/3}/\mu kT)(b/d) \qquad (13)$$

where b is the Burgers vector, Ω the molecular volume and D_b the grain boundary diffusion coefficient.

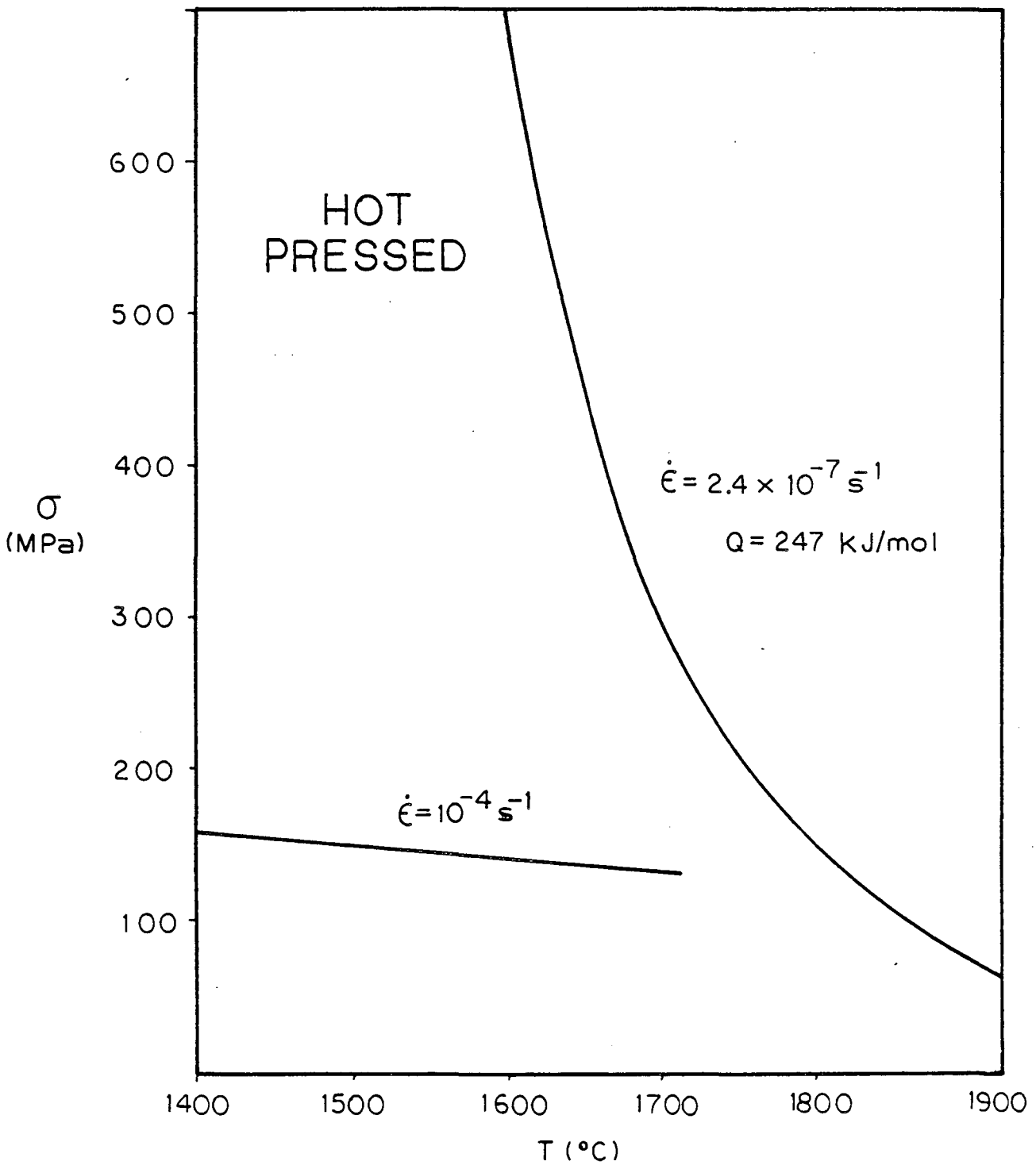
HOT
PRESSED
$\dot{\epsilon} = 2.4 \times 10^{-7}\ s^{-1}$
Q = 247 kJ/mol
$\dot{\epsilon} = 10^{-4}\ s^{-1}$
σ
(MPa)
600
500
400
300
200
100
1400
1500
1600
1700
1800
1900
T (°C)

FIG. 26

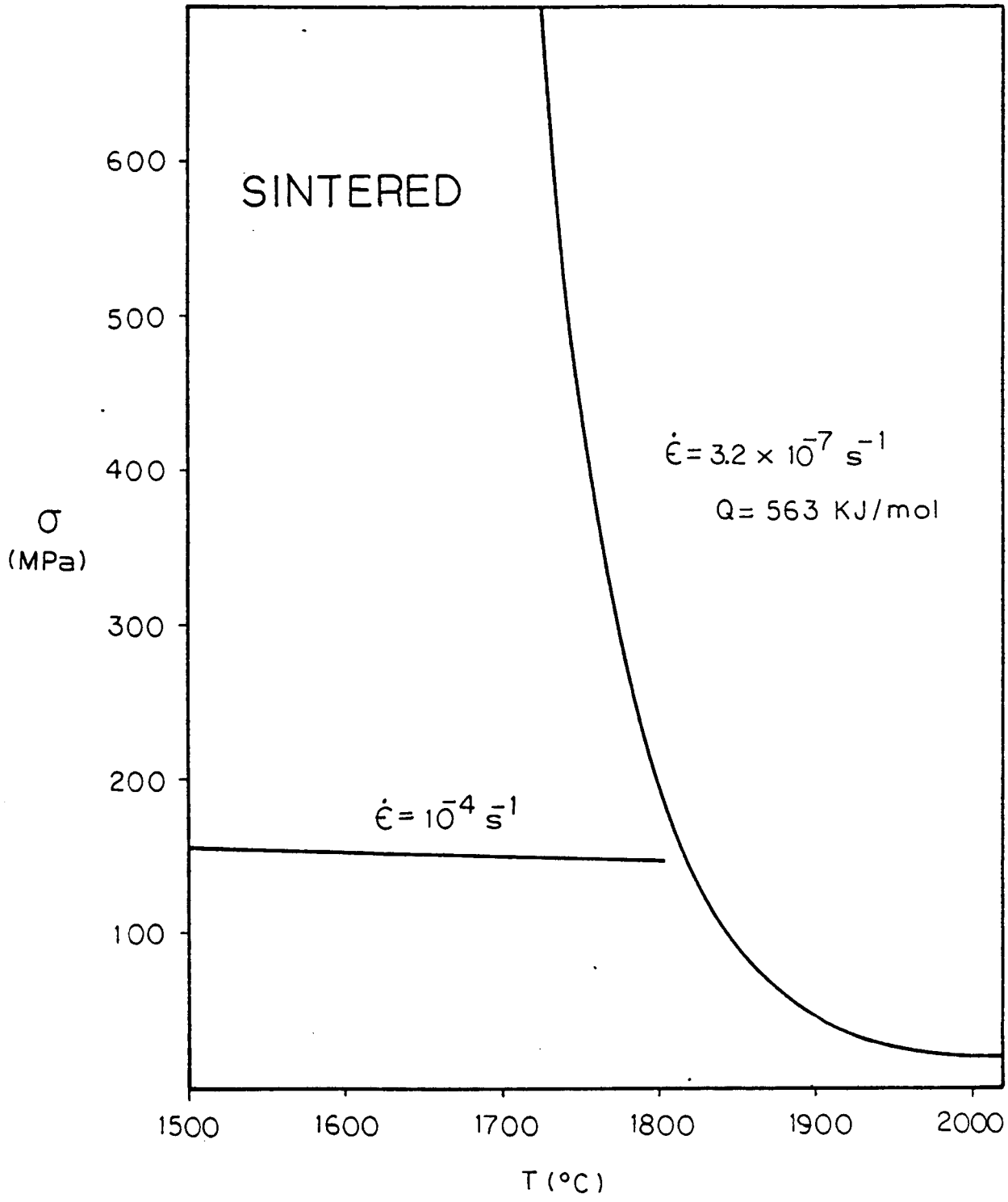
SINTERED
600
500
400
300
200
100
σ
(MPa)
$\dot{\epsilon} = 3.2 \times 10^{-7}\ s^{-1}$
Q= 563 KJ/mol
$\dot{\epsilon} = 10^{-4}\ s^{-1}$
1500
1600
1700
1800
1900
2000
T (°C)

FIG. 27

4.2 The Fracture Stress

The onset of crack blunting at elevated temperature clearly changes the brittle fracture process. Prediction of trends in the brittle fracture stress with temperature thus requires that both the operative fracture mechanism in the presence of a blunt crack be established and the rate of blunting be ascertained. Analysis of the tests performed at room temperature on cracks subjected to high temperature blunting provides some information pertinent to these issues.

The present premise is that fracture from blunt cracks is governed by the peak tensile stress in the crack field, $\hat{\sigma}$ (Fig. 19). This stress may be derived from the measured strength S using Eq. (15), and then using K to estimate the size of the microstructural flaw needed to cause failure; $a_c \approx (\pi/4)(K_c/\hat{\sigma})^2$. This procedure suggests flaws ~12μm in diameter, comparable to the size of the voids observed in the crack tip region. The present hypothesis, therefore, is that the voids are fracture sites and hence that trends in the fracture stress are governed by variations in the peak stress with blunting and by the growth of voids in the crack tip damage zone.

Detailed considerations of trends in fracture stress would include statistical considerations comparable to those used to describe the brittle-to-ductile transition in steels.[29,30] Insufficient information exists for this purpose. Nevertheless, some insight can be gained by noting the trend in the peak stress during high temperature testing, obtained from Eqs. (6) and (9), viz,

$$\hat{\sigma}/\sigma_{\infty} \approx 0.93/\sqrt{\varepsilon_{\infty}} \tag{14}$$

Furthermore, during a typical test, the stress and strain vary as Fig. (28);

$$\varepsilon_{\infty} \approx \varepsilon_{ss} \tan[(\pi/2)(\sigma_{\infty}/\sigma_{ss})] \tag{15}$$

where the subscript ss refers to steady-state flow. Combination of Eqs. (14) and (15) reveals a maximum in $\hat{\sigma}$, which occurs when $\sigma_{\infty} \approx 0.55\ \sigma_{ss}$. Consequently when the steady-state creep stress becomes less than about 1.4 times the fracture stress, creep ductility is assured.

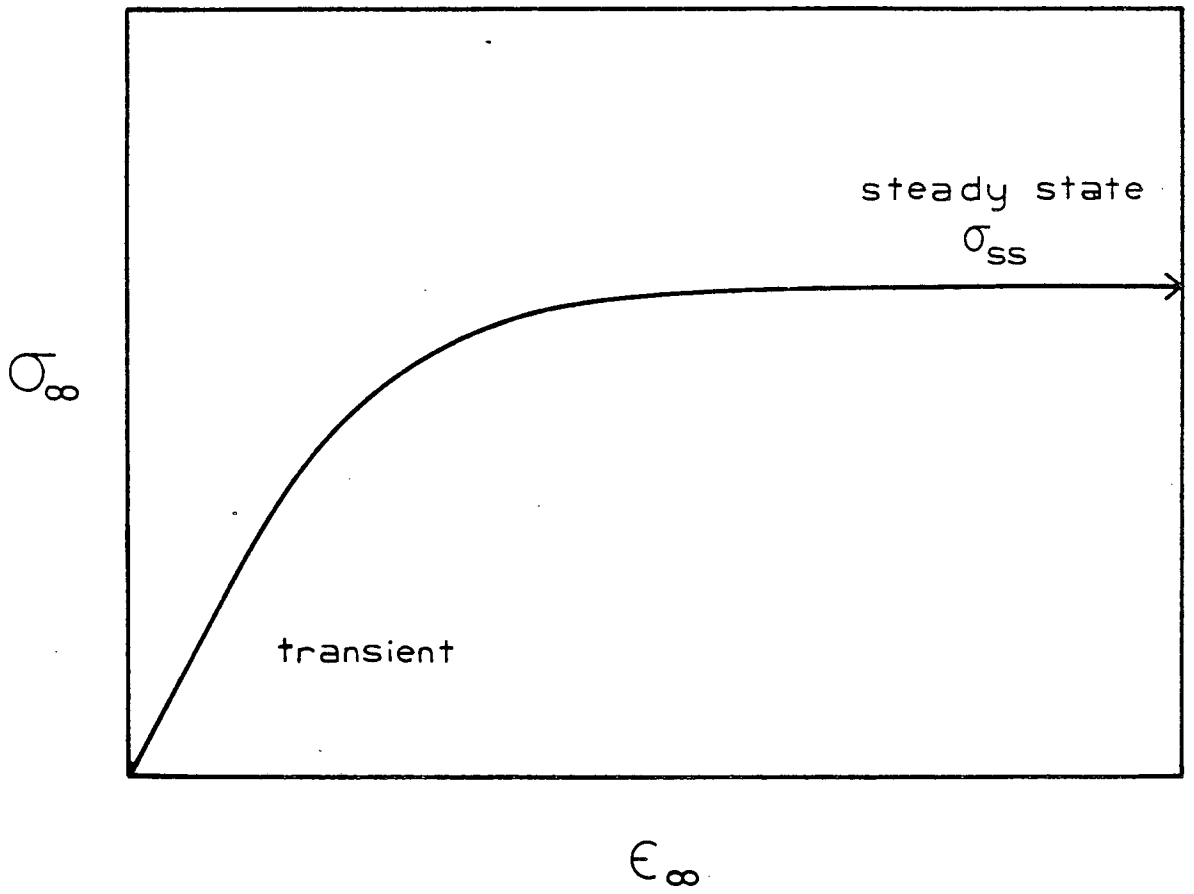

FIG. 28

5. CONCLUSIONS

Silicon carbide exhibits a transition from creep-brittleness to creep-ductility. Below the transition temperature the material fails by brittle crack extension. Above the transition temperature the material is superplastic and can withstand strains in excess of 10%. Indentation cracks above the transition temperature in sintered silicon carbide open and blunt with damage around the crack tip characterized by cavities opening at graphite inclusions. The indentation cracks in the hot-pressed material open, stay sharp, and propagate at a very slow rate with cavity formation on grain facets in front of the crack tip.

The brittle fracture stress of silicon carbide at rapid strain rates is temperature insensitive. However, the deformation stress is strongly dependent on strain rate and temperature. The blunting rate is a deformation process that determines whether the crack will extend. If a crack blunts readily the stress field around its tip is reduced, therefore preventing brittle fracture. Constant strain rate deformation creates a maximum peak stress ahead of a crack tip when the applied stress reaches slightly more than half the flow stress. If the material can survive this point it will continue to deform to large strains.

References

1. Dalgleish, B.J., Johnson, S.M. and Evans, A.G., "High-Temperature Failure of Polycrystalline Alumina: I, Crack Nucleation," Journal of the American Ceramic Society, Vol. 67, No. 11, Nov. 1984, pp. 741-750.

2. Blumenthal, W. and Evans, A.G., "High-Temperature Failure of Polycrystalline Alumina: II, Creep Crack Growth and Blunting," Journal of the American Ceramic Society, Vol. 67, No. 11, Nov. 1984, pp. 751-759.

3. Johnson, S.M., Dalgleish, B.J. and Evans, A.G., "High Temperature Failure of Polycrystalline Alumina: III, Failure Times," Journal of the American Ceramic Society, Vol. 67, No. 11, Nov. 1984, pp. 759-763.

4. Dalgleish, B.J. and Evans, A.G., "Influence of Shear Bands on Creep Rupture in Ceramics," Journal of the American Ceramic Society, Vol. 8, No. 1, January 1985, pp. 44-48.

5. Dalgleish, B.J., Slamovich, E.B. and Evans, A.G., "Duality in the Creep Rupture of a Polycrystalline Alumina," Journal of the American Ceramic Society, Vol. 68, No. 11, November 1985, pp. 575-581

6. Jakus, K., Weiderhorn, S.M. and Hockey, B.J., "Nucleation and Growth of Cracks in Vitreous-Bonded Aluminum Oxide at Elevated Temperatures," Journal of the American Ceramic Society, Vol. 69, No. 10, October 1986, pp. 725-731.

7. McHenry, K.D. and Tressler, R.E., "High Temperature Dynamic Fatigue of Hot-Pressed SiC and Sintered-SiC," American Ceramics Society Bulletin, Vol. 59, No. 4, April 1980, pp. 459-461.

8. McHenry, K.D. and Tressler, R.E., "Fracture Toughness and High Temperature Slow Crack Growth in SiC," Journal of the American Ceramic Society, Vol. 63, No. 3-4, March-April, 1980, pp. 152-156.

9. Minford, E.J. and Tressler, R.E., "Determination of Threshold Stress Intensity for Crack Growth at High Temperature in Silicon Carbide Ceramics," Journal of the American Ceramic Society, Vol. 66, No. 5, May 1983, pp. 338-340.

10. Minford, E.J., Kupp, D.M. and Tressler, R.E., "Static Fatigue Limit for Sintered Silicon Carbide at Elevated Temperatures," Journal of the American Ceramic Society, Vol. 66, No. 11, November 1983, pp. 769-773.

11. Grathwohl, G., "Regimes of Creep and Slow Crack Growth in High-Temperature Rupture of Hot-Pressed Silicon Nitride," Deformation of Ceramic Materials II, ed. by Tressler, R.E. and Bradt, R.C., Plenum Press, New York, 1984, pp. 573-586.

12. Evans, A.G., Rice, J.R. and Hirth, J.P., "Suppression of Cavity Formation in Ceramics: Prospects for Superplasticity," Journal of the American Ceramic Society, Vol. 63, No. 7-8, July-August 1980, pp. 368-375.

13. Wakai, F., Sakaguchi, S. and Kato, H., "Compressive Deformation Properties and Microstructures in the Superplastic Y-TZP," Journal of the Ceramic Society of Japan, Vol. 94, No. 8, 1986, pp. 721-725.

14. Wakai, F., Kato, H., Sakaguchi, S. and Murayama, N., "Compressive Deformation of Y_2O_3-Stabilized ZrO_2/Al_2O_3 Composite," Journal of the Ceramic Society of Japan, Vol. 94, No. 9, 1986, pp. 1017-1020.

15. Kellett, B.J. and Lange, F.F., "Hot Forging Characteristics of Fine-Grained ZrO_2 and Al_2O_3/ZrO_2 Composites," Communications of the American Ceramic Society, August 1986, pp. C172-C173.

16. Kellett, B.J. and Lange, F.F., "Hot Forging Characteristics of Transformation Toughened Al_2O_3/ZrO_2 Composites," Journal of Materials Research, in press.

17. Weaver, G.Q. and Olson, B.A. (Norton Co.), "Sintered Silicon Carbide," U.S. Pat. 3836673, September 17, 1974.

18. Coppola, J.S. and Smoak, R.H. (Carborundum Co.), "Method of Producing High Density Silicon Carbide Product," U.S. Pat. 4080415, March 21, 1978.

19. Prochaska, S., "Ceramics for High Temperature Applications," edited by J.J. Burke, A.E. Gorun and R.N. Katy, Brook Hill Publishing Co., Chestnut Hill, MA, 1974, p. 239.

20. Ruska, J., Gauckler, L.I., Loreny, J. and Rexer, H.V., "The Quantitative Calculation of SiC Polytypes from Measurements of X-ray Diffraction Peak Intensities," Journal of Materials Science, Vol. 14, 1979, pp. 2013-2017.

21. Paris, P.C. and Sih, G.C., "Stress Analysis of Cracks," from Fracture Toughness Testing and its Applications, ASTM STP 381, 1965, pp. 30-81.

22. Kingery, W.D., Bowen, H.K. and Uhlmann, D.R., Introduction to Ceramics, 2nd Ed., John Wiley & Sons, New York, 1976, p. 708.

23. Hollenberg, G.W., Terwilliger, G.R. and Gordon, R.S., "Calculation of Stresses and Strains in Four-Point Bending Creep Tests," Journal of the American Ceramic Society, Vol. 54, No. 4, April 1971, pp. 196-199.

24. Riedel, H. and Rice, J.R., "Tensile Cracks in Creeping Solids," Fracture Mechanics: Twelfth Conference, ASTM STP 700, 1980, pp. 112-130.

25. Hutchinson, J.W., "Singular Behavior at the End of a Tensile Crack in a Hardening Material," Journal of the Mechanics and Physics of Solids, Vol. 16, 1968, pp. 13-31.

26. McMeeking, R.M., "Finite Deformation Analysis of Crack-Tip Opening in Elastic-Plastic Materials and Implications for Fracture," Journal of the Mechanics and Physics of Solids, Vol. 25, 1977, pp. 357-381.

27. Packer, C.M. and Sherby, O.D., "An Interpretation of the Superplasticity Phenomenon in Two-Phase Allows," Transactions of the ASM, Vol. 60, 1967, pp. 21-28.

28. Raj, R. and Baik, S., "Creep Crack Propagation by Cavitation Near Crack Tips," Metal Science Journal, August-September 1980, pp. 385-394.

29. Tsann Lin, Evans, A.G. and Ritchie, R.O., "A Statistical Model of Brittle Fracture by Transgranular Cleavage," Journal of the Mechanics and Physics of Solids, Vol. 34, No. 5, 1986, pp. 477-497.

30. Tsann Lin, Evans, A.G. and Ritchie, R.O., "Statistical Analysis of Cleavage Fracture Ahead of Sharp Cracks and Rounded Notches," Acta Metallurgica, Vol. 34, No. 11, 1986, pp. 2205-2216.

This report was done with support from the Department of Energy. Any conclusions or opinions expressed in this report represent solely those of the author(s) and not necessarily those of The Regents of the University of California, the Lawrence Berkeley Laboratory or the Department of Energy.

Reference to a company or product name does not imply approval or recommendation of the product by the University of California or the U.S. Department of Energy to the exclusion of others that may be suitable.

LAWRENCE BERKELEY LABORATORY
TECHNICAL INFORMATION DEPARTMENT
UNIVERSITY OF CALIFORNIA
BERKELEY, CALIFORNIA 94720